Characterization and suppression of the hydrodynamic instability in the time domain for acoustic propagation in a lined flow duct

Yuanyuan Deng, Antoni Alomar, Didier Dragna, Marie-Annick Galland

Version of Record: https://www.sciencedirect.com/science/article/pii/S0022460X21000717
Manuscript_3638d1d73f9e671be6da3234f0f11602

Characterization and suppression of the hydrodynamic instability in the time domain for acoustic propagation in a lined flow duct

Yuanyuan Deng, Antoni Alomar, Didier Dragna, Marie-Annick Galland

Universite de Lyon, Ecole Centrale de Lyon, INSA Lyon, UCB Lyon 1, CNRS LMFA UMR 5509
36 Av Guy de Collongue, Ecully 69134, France

Abstract

The gradient term suppression (GTS) method for removing the hydrodynamic instability appearing in the time-domain solutions of the linearized Euler equations (LEE) along a lined flow duct is assessed. For this, the characterization of a convective instability in the time domain, with the aid of a complementary modal analysis, is first presented. The effect of the mesh size and spatial filtering on the instability is investigated. In particular, a convergence of the instability in the time domain is achieved for a small enough grid size. The consequence of suppressing the mean flow gradient term on the modes is then investigated. It is shown that the unstable modes are indeed removed, but also that acoustic modes are significantly modified, especially for low Helmholtz numbers. The GTS method is finally applied to the NASA grazing impedance tube benchmark. It is found that tuning the weight of the mean flow gradient term within the LEE can be effective for suppressing the instability while conserving a reasonable accuracy of the acoustic component.

Keywords: Lined flow duct, hydrodynamic instability, removing of instability, time domain

1. Introduction

Acoustic liners are widely used in the intake or bypass of the aero-engines to attenuate the noise generated by airplanes. To study their interaction with acoustic waves in the presence of a mean flow, time-domain approaches, based on the linearized Euler equations (LEE), are well-suited, as broadband results can be obtained with a single simulation [1, 2, 3]. In addition, extension to account for nonlinear effects due to large sound pressure levels can be considered. Time-domain approaches are however especially sensitive to instabilities, which can contaminate the pressure field and complicate the extraction of the acoustic component.

The presence of an instability over acoustic liners was first detected experimentally through the transmission coefficient [4, 5, 6, 7]. The transmission coefficient became larger than 1 around the liner resonance at sufficiently high Mach numbers, implying a source of acoustic energy. The source was rightfully attributed to an instability. Optical flow measurements [8, 9] led to a full spatial characterization of the instability, and revealed its convective nature.

The use of the Ingard-Myers boundary condition [10, 11], which describes how acoustic perturbations interact with an impedance wall for a vanishingly-thin inviscid boundary layer, was the

Email addresses: yuanyuan.deng@ec-lyon.fr (Yuanyuan Deng), tonignasi@gmail.com (Antoni Alomar), didier.dragna@ec-lyon.fr (Didier Dragna), marie-annick.galland@ec-lyon.fr (Marie-Annick Galland)

usual approach from the early numerical and theoretical works on the subject. By doing so, instabilities were observed in many studies [12, 13, 1, 14, 15, 16]. Later, Brambley [17] showed that the Ingard-Myers boundary condition is mathematically ill-posed in the time domain because the model supports unstable modes of unlimited exponential growth at arbitrarily short wavelengths. He [18] has shown later theoretically that accounting for a boundary layer thickness in the boundary condition (modified Ingard-Myers condition) regularizes the problem. Since many studies have questioned the validity of the Ingard-Myers boundary condition [19, 20], the use of a finite boundary layer thickness has been explored to improve the modeling of the instabilities [21, 22, 23, 24, 25, 26]. Detailed numerical analysis with a mass-spring-damper impedance model showed that the use of a mean velocity profile instead of the Ingard-Myers condition transformed the unstable mode from absolute to convective [27]. However, even with a full velocity profile, absolute instabilities seems to be present in time-domain simulations for liners with a more realistic broadband impedance [28].

The thermoviscous effects [29] or turbulent dissipation through an eddy viscosity profile [30, 31, 32] are capable of attenuating the instability. It can even lead the nature of instability to change from absolute to convective [30, 29]. Including turbulent dissipation, the properties of the instability appear to be close to the experimental results. More recently, numerical simulations of a channel flow with an acoustic liner using implicit large eddy simulations [33] were performed. Surface waves with characteristics similar to the instability predicted by linear stability analysis were exhibited. However, very fine grids, and even tremendous computational resources for direct numerical simulations, are needed in those studies to properly capture the instability, which is a strong disadvantage if the goal of the simulations is the computation of the acoustic field.

Various strategies to attenuate the instability numerically in time-domain simulations have been explored in the past. Since it is observed that the instability often appears in fine grids, the use of coarse grids and artificial damping has been recommended to attain a stable simulation by some authors. In particular, the studies of Gabard and Brambley [27, 34] suggest that the origin of the absolute instability lies in the dispersion properties of the finite-difference schemes, and they proved the effectiveness of numerical filtering at the boundary to avoid spurious numerical instabilities. Marx [25] examined the case of a convective instability in the time-domain, and assessed the impact of selective filtering and grid size. He considers that if the instability is physical, increasing the grid size or strengthening the selective filters do not necessarily attenuate the instability.

Another approach, widely used in flows reminiscent of shear instabilities, is the substitution of the underlying LEE by a new set of equations which are inherently stable. Among them we can mention the gradient term suppression method (GTS) [35, 36, 37, 38, 39], the acoustic perturbation equations [40], the linearized perturbed compressible equations [41, 42], or the gradient term filtering method [43, 44]. These methods have been applied to deal with Kelvin-Helmholtz (KH) instabilities in various cases with shear flows, such as sound radiation through two-dimensional shear layers and sound radiation from a bypass duct[44, 36]. It has been shown that most of them are similarly effective for these particular flows [44].

To the authors' knowledge, such methods have not been employed yet for the suppression of instabilities generated in a lined flow duct. It is worth mentioning that the mechanism for these instabilities, while related to KH instabilities, is different. Specifically, the instabilities in a lined flow duct are related to the presence of acoustic liners and not only due to the shear flow. Among the methods existing in the literature for KH instabilities, we have opted to restrict ourselves to GTS in this study, as a first approach to the case of acoustic liners. However, other methods might perform similarly or even better in certain cases, so a future comparative study would certainly be

useful.

The objective of the paper is to analyze the effectiveness of the GTS method in suppressing the hydrodynamic instability that appears in the time-domain simulations of acoustic propagation along a lined duct. For this, it is beforehand verified that the instability is not of numerical origin and is a part of the LEE solution and that its characteristics are in good agreement with the predictions of a reference modal analysis, following Marx [25]. In particular, the impact of the grid resolution and the amount of selective filtering on instabilities are analyzed.

The paper is organized as follows. The configuration of the model, the governing equations and the numerical schemes are presented in Section 2. An example of an instability in the time-domain approach is shown and is characterized in Section 3. In Section 4, the effect of the selective filter and mesh size on the instability is assessed. Finally, in Section 5, the performance of the partial GTS method to suppress the instability is analyzed, and is applied on the NASA GIT benchmark problem.

2. Numerical models

A two-dimensional partially lined duct, of size $H \times L$, is considered, as shown in Fig. 1. The acoustic liner is installed on the upper wall, while the lower wall is rigid. A point source is fixed in the center of the duct. The source is impulsive, unless stated otherwise. A parallel shear flow of velocity profile u_0 goes from left to right, and vanishes on the walls. ρ_0 is the mean density, and c_0 is the sound speed. The physical quantities with dimensions of length, time, velocity, and pressure are nondimensionalized using H, H/c_0, c_0 and $\rho_0 c_0^2$, respectively.

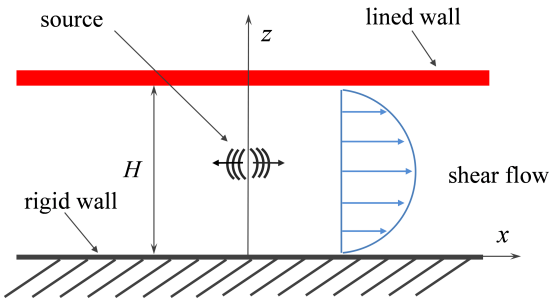

Fig. 1. Numerical configuration.

2.1. Governing equations

Acoustic propagation in a lined flow duct is governed by the LEE. Assuming the mean flow is homentropic and neglecting the gradient of mean pressure, the LEE in dimensionless form are written as:

$$\frac{\partial p}{\partial t} + u_0 \frac{\partial p}{\partial x} + \frac{\partial u}{\partial x} + \frac{\partial v}{\partial z} = Q \tag{1a}$$

$$\frac{\partial u}{\partial t} + u_0 \frac{\partial u}{\partial x} + v \frac{\mathrm{d}u_0}{\mathrm{d}z} + \frac{\partial p}{\partial x} = 0 \tag{1b}$$

$$\frac{\partial v}{\partial t} + u_0 \frac{\partial v}{\partial x} + \frac{\partial p}{\partial z} = 0 \tag{1c}$$

where p, u and v are the acoustic pressure and components of the acoustic velocity along the x and z-direction, respectively.

The mean flow velocity profile is given by:

$$u_0(z) = M\frac{n_t+1}{n_t}\left(1-|1-2z|^{n_t}\right), \tag{2}$$

where M is the Mach number corresponding to the mean velocity. The parameter n_t specifies the flow profile and can be related to the boundary layer thickness. The displacement thickness, defined by:

$$\delta = \int_0^{1/2}\left(1-\frac{u_0(z)}{u_0(1/2)}\right)\mathrm{d}z \tag{3}$$

is equal to $\delta = 1/[2(n_t+1)]$. Unless stated otherwise, the flow profile parameter is set to $n_t = 9$, corresponding to $\delta = 5$ %. Note the 2D velocity profile in Eq. (2) does not have an inflection point and should not support any KH instability. While not shown for conciseness, it has been verified that the time-domain simulations in a rigid duct with this sheared flow profile do not present any instability.

2.2. Time-domain solver

The LEE are solved using high order finite-difference time-domain methods. The spatial derivatives are calculated by optimized 4th-order finite-difference schemes over 11 points. Namely, the centered scheme of Bogey & Bailly [45] and the non-centered schemes of Berland *et al.* [46] are employed for the interior and boundary points, respectively. The optimized, 4th-order 6-stage Runge-Kutta algorithm of Berland *et al.* [47] is employed for time integration. The time step is $\Delta t = 0.0014$.

Selective filters are used to remove grid-to-grid oscillations. For the interior points, the centered 11-point 6th-order selective filter of Bogey *et al.* [48] is adopted. For the boundary points, the selective filters of Berland *et al.* [46] are used. A parameter, denoted by σ and referred to as the filtering strength, allows one to adjust the effect of the selective filters. It ranges from 0 to 1, 0 meaning that no filtering is applied and 1 meaning that grid-to-grid oscillations are totally removed. As the filtering is applied at every iteration, a filtering strength of 1 is usually not necessary and can even deteriorate longer, well-resolved wavelengths. The default value is $\sigma = 0.5$.

The mesh is uniform in the x-direction with a size of $\Delta x = 0.02$. This ensures that the number of points per acoustic wavelength $\lambda = 2\pi/\omega$ is larger than 10 up to $\omega = 10\pi$. It can be noticed that the duct cut-off frequency in the no-flow case corresponds to $\omega = \pi$. Damping zones with a length of 20, are implemented upstream and downstream to prevent reflections. In these zones, the mesh spacing gradually increases with a stretching factor of 3% and a Laplacian filter is applied to add artificial dissipation [49]. Along the z-direction, the mesh size decreases gradually towards the walls with a shrinking factor of 1%. The number of grid points along the duct height is n_z, with default value 175.

For the rigid wall, the boundary condition $v_z(x, z=0) = 0$ is imposed. The lined wall is modelled through the impedance boundary condition:

$$p(x, z=1, t) = [\tilde{z} * v_n](x, t), \tag{4}$$

where $*$ denotes the convolution operator, $v_n(x,t) = v(x, z=1, t)$ and $\tilde{z}(t)$ is the impedance model

in the time domain. To avoid computing the convolution integral, the time-domain boundary condition proposed in Troian *et al.* [50] is employed. For this, the admittance in the frequency domain $\beta(\omega)$, related to the time-domain impedance model by

$$\beta(\omega)^{-1} = \int_{-\infty}^{+\infty} \tilde{z}(t) \mathrm{e}^{-\mathrm{i}\omega t} \mathrm{d}t, \tag{5}$$

is approximated by a rational function:

$$\beta(\omega) = Y_\infty + \sum_{i=1}^{P} \frac{A_i}{\lambda_i + \mathrm{i}\omega} + \sum_{i=1}^{S} \left(\frac{B_i - \mathrm{i}C_i}{\alpha_i - \mathrm{i}\beta_i + \mathrm{i}\omega} + \frac{B_i + \mathrm{i}C_i}{\alpha_i + \mathrm{i}\beta_i + \mathrm{i}\omega} \right), \tag{6}$$

where λ_i and $\alpha_i \pm \mathrm{i}\beta_i$ are respectively the real poles and complex-conjugate pole pairs of $\beta(\omega)$, P and S denote their number and Y_∞, A_i, B_i and C_i are real coefficients. For a given broadband impedance model, the admittance parameters in Eq. (6) are determined using the vector fitting algorithm [51] in the frequency band of interest. The implementation of the time-domain impedance boundary condition is not further described here but interested readers can refer to Troian *et al.* [50] for details.

The source term Q in Eq. (1a) is chosen as

$$Q(x, z, t) = \lambda(t) \exp\left(-\frac{x^2 + (z - 0.5)^2}{B_s^2} \ln 2 \right), \tag{7}$$

where B_s is the Gaussian half-width of the source, with a value of 0.104. Both impulsive and harmonic sources are used in this study. For impulsive sources, $\lambda(t)$ is defined as:

$$\lambda(t) = \frac{t - t_s}{t_c} \exp\left(-\frac{(t - t_s)^2}{t_c^2} \ln 2 \right) H(t) \tag{8}$$

where $t_s = 5.42$ is a time shift, $t_c = 0.95$ specifies the frequency content of the source signal and $H(t)$ is the Heaviside function. In the case of a harmonic source $\lambda(t)$ is defined as:

$$\lambda(t) = \exp(\mathrm{i}\omega t) H(t) \tag{9}$$

with ω the angular frequency. A complex-valued harmonic source is chosen for an easier extraction of instability characteristics. It can be noticed that acoustic pressure and velocity fields in the time-domain numerical simulations are also complex-valued when this harmonic source is employed.

2.3. Modal analysis approach

A modal analysis is also performed to determine the stability properties of the lined section, from which the wavenumbers and the mode shapes of all modes can be determined, including the unstable modes. Monochromatic waves propagating in an infinite, homogeneous duct are considered:

$$\begin{aligned} u &= U(z) \, \mathrm{e}^{\mathrm{i}(\omega t - kx)}, \\ v &= V(z) \, \mathrm{e}^{\mathrm{i}(\omega t - kx)}, \\ p &= P(z) \, \mathrm{e}^{\mathrm{i}(\omega t - kx)}, \end{aligned} \tag{10}$$

where U, V and P are the mode shapes, which depend only on z, and k is the mode wavenumber. Note that ω and k can be complex-valued.

In order to obtain this information, the next step is to introduce Eqs. (10) into Eqs. (1) to obtain an eigenvalue problem. The eigenvalue problem is not directly formulated using the physical variables; instead, the characteristic variables, i.e., U, $P-V$ and $P+V$, are used. Specifically, $P-V$ and $P+V$ are the characteristic waves travelling along the $-z$ and $+z$-direction, respectively. The motivation for using the characteristic variables is described below. The discretization of the LEE on a grid with N points leads to a system of $3N$ equations for $3N$ unknowns. The boundary conditions however bring two additional equations. In order to avoid having an overdetermined system, it is thus necessary to choose two equations to eliminate, which is not trivial and somewhat arbitrary. The characteristic variables allow for a suitable choice (see Appendix A).

Doing so, the LEE in the frequency domain are written as:

$$\begin{pmatrix} 1 & \dfrac{-1}{2\mathrm{i}\omega}\dfrac{\mathrm{d}u_0}{\mathrm{d}z} & \dfrac{1}{2\mathrm{i}\omega}\dfrac{\mathrm{d}u_0}{\mathrm{d}z} \\ 0 & 1-\dfrac{1}{\mathrm{i}\omega}\dfrac{\mathrm{d}}{\mathrm{d}z} & 0 \\ 0 & 0 & 1+\dfrac{1}{\mathrm{i}\omega}\dfrac{\mathrm{d}}{\mathrm{d}z} \end{pmatrix} \begin{pmatrix} U \\ P-V \\ P+V \end{pmatrix} = \frac{k}{\omega} \begin{pmatrix} u_0 & \frac{1}{2} & \frac{1}{2} \\ 1 & u_0 & 0 \\ 1 & 0 & u_0 \end{pmatrix} \begin{pmatrix} U \\ P-V \\ P+V \end{pmatrix}. \tag{11}$$

This matrix system has to be completed with appropriate boundary conditions. On the rigid wall, the boundary condition becomes $[P+V](z=0) = [P-V](z=0)$. On the lined wall, the impedance boundary condition is written as:

$$[P-V](z=1) = \frac{1-\beta}{1+\beta}[P+V](z=1) \tag{12}$$

Note that the admittance in Eq. (12) depends on the frequency. In the stability analysis performed in Section 3, the frequency can be complex-valued and the admittance has to be calculated accordingly. To be noticed, admittance models given by a rational function in Eq. (6) are used in the paper.

The eigenvalue problem in Eq. (11) is solved numerically. The spatial derivatives are discretized using the Chebyshev spectral method [52], which is able to generate smaller numerical errors than finite-difference schemes for a given number of grid points. The gradient of the mean flow $\mathrm{d}u_0/\mathrm{d}z$ is also calculated numerically using the Chebyshev spectral method. The default value of the number of grid points N used in the modal analysis is 150. The discretized LEE are then recast into a generalized eigenvalue problem, which is solved by the `eig` function of *MATLAB*. Details on the discretization and on the implementation of boundary conditions are provided in Appendix A.

3. Stability analysis

As described in the previous section, both methods will be applied to study hydrodynamic instabilities. The occurrence of a hydrodynamic instability depends on the characteristics of the liner, the mean flow profile and the source frequency. Two cases with Mach numbers of $M = 0.1$ and $M = 0.3$ are considered. The corresponding flow profiles are shown in Fig. 2. For simplicity, a

mass-spring-damper (MSD) liner is used, with impedance

$$Z(\omega) = R + \mathrm{i}\omega m + \frac{K}{\mathrm{i}\omega}, \tag{13}$$

where R, m and K are respectively the damping, mass and spring stiffness. The impedance spectrum of the liner used in our case is shown in Fig. 3, with $R = 0.2$, $m = 5.4 \times 10^{-3}$ and $K = 0$.

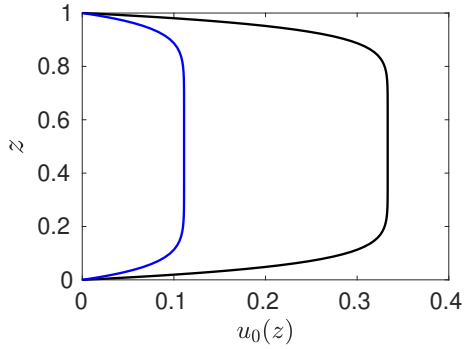

Fig. 2. Mean flow profile for: $M = 0.1$ and $M = 0.3$.

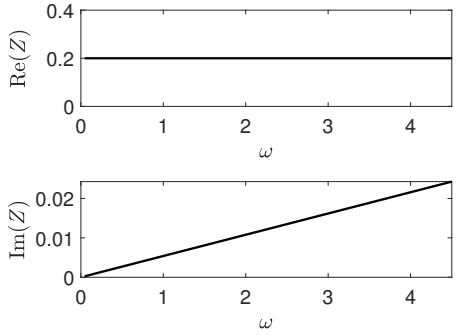

Fig. 3. Impedance of the MSD liner.

3.1. Example of time-domain simulation

Time-domain simulations are first performed using an impulsive source to illustrate the acoustic propagation along the lined duct. Fig. 4 shows the pressure response varying with time and position along the x-axis on the lined wall. For $M = 0.1$, two branches originating from $t = t_s$ are observed, corresponding to upstream and downstream propagating waves. These acoustic waves are attenuated along the lined wall. After $t \approx 18$, they have left the computational domain and the remaining fluctuating pressure is almost null. For $M = 0.3$, these two branches are retrieved. Their orientation is modified due to the difference in the Mach number. Another contribution is however observed in the downstream direction. Its magnitude and its spatial extent increase as it propagates away from the source, indicating it is an instability. Moreover, since the pressure response is given as a function of the distance and time, the velocity of acoustic waves and instabilities can be

deduced from the slopes of the different branches. It can then be estimated that the propagation velocity of the instability is smaller than that of the acoustic waves.

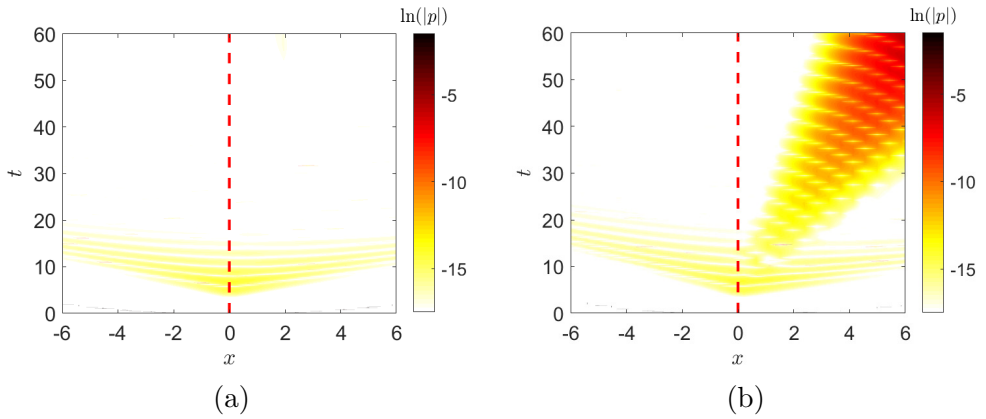

Fig. 4. Pressure response $\ln|p(x, z = 1, t)|$ to an impulsive source on the lined wall for (a) $M = 0.1$ and (b) $M = 0.3$. The source position is indicated by the vertical dashed line.

3.2. Characterization of the instability from modal analysis

This section aims at correlating the instability observed in the time-domain simulations with the modal analysis. Therefore, a harmonic source is imposed on both approaches. For predicting the response to a harmonic excitation, a spatial stability analysis is performed: the frequency is real-valued and the mode wavenumbers can be complex. Fig. 5 displays the wavenumbers of all modes at $\omega = 0.9271$ for both $M = 0.1$ and $M = 0.3$. This particular frequency is chosen because it corresponds to a dimensional frequency $f = 1000$ Hz for the benchmark data of the NASA GIT duct (sound speed $c_0 = 344.28$ m s^{-1} and duct height $H = 0.0508$ m), which is considered in Section 5.3. It is also close to the frequency $\omega = 0.8344$ where the maximal spatial growth rate is observed (not shown). For $M = 0.1$, there is no mode in the upper-right complex k-plane and therefore no possible instability. For $M = 0.3$, the wavenumber of one mode ($k = 6.78 + 1.97$i) has both positive real and imaginary parts. This is possibly an unstable mode, and its stability depends on the propagation direction. If the mode is an upstream decaying mode, the propagation is stable. On the other hand, if it propagates in the downstream direction, it corresponds to an instability. The propagation direction of this mode therefore needs to be determined.

In Fig. 5, noticeable modes other than the acoustic modes and the instability are convected modes which satisfy the dispersion relation $ku_0(z) = \omega$. For a sheared mean flow, they come as a continuous spectrum, located in the k-plane along the horizontal half-line starting at $k = \omega/\max(u_0)$. In solving numerically the eigenvalue problem, this continuous spectrum turns into individual modes, which are greatly dependent on the discretization. In particular, even the wavenumbers of these modes may have small positive imaginary parts and thus be weakly unstable. As shown in the study of Brambley *et al.* [53], the contributions of the continuous spectrum are negligible when the point source is located at the duct centerline, where the mean flow is relatively unsheared. Note that the use of selective filters, as employed in the time-domain simulations, tends to move the convected modes towards the lower right quadrant of the k-plane [25] and thus to make all these modes stable. As we are primarily interested in the instability, no specific method is employed to

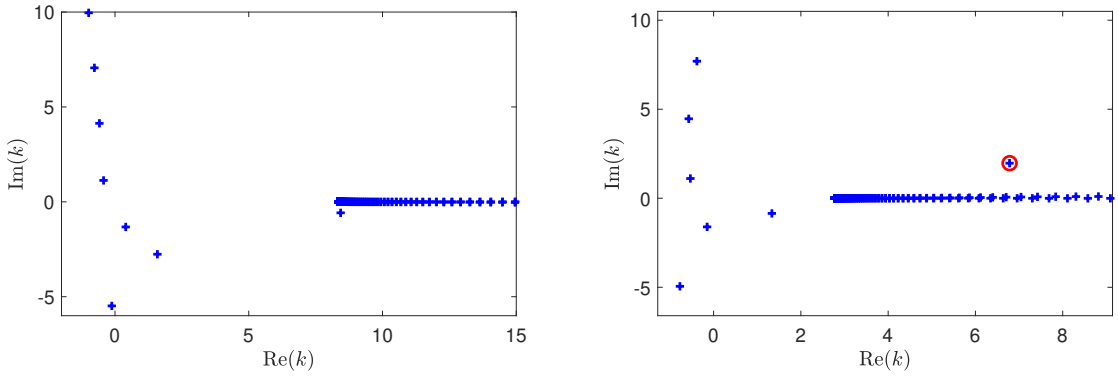

Fig. 5. Wavenumber obtained from modal analysis for $\omega = 0.9271$ and for (a) $M = 0.1$ and (b) $M = 0.3$. The encircled wavenumber indicates a possible unstable hydrodynamic mode.

have an accurate prediction of convective modes. Such a method has been for instance described in Vilenski and Rienstra [54].

The Briggs-Bers criterion [55, 56] is used to determine the propagation direction of the modes, and, if an unstable mode is present, whether it is convective or absolute. This criterion has been introduced to study the plasma instability and has been later considered for the stability analysis of acoustic propagation in a lined flow duct [17]. However, before using the Briggs-Bers criterion, it must be checked that it is applicable. For instance, as discussed by Brambley [17], the acoustic propagation in a lined duct with a plug flow and the Myers impedance boundary condition is mathematically ill-posed, implying that Briggs-Bers criterion can not be used. In order to apply the Briggs-Bers criterion, one must first check that the growth rates of all modes, and in particular the unstable modes, are bounded. To do so, a temporal stability analysis is conducted. The wavenumber here remains real, and the frequency ω, possibly complex-valued, satisfying the dispersion relation is sought. If for a particular value of the wavenumber, one has $\mathrm{Im}(\omega) < 0$, the system is then unstable. Fig. 6 shows the growth rate of the possible unstable mode for $M = 0.3$ as a function of $\mathrm{Re}(\omega)$. It is observed that the growth rate is bounded at $\mathrm{Im}\,(\omega) \approx -0.23$, meaning that the instability will not be amplified at an arbitrarily large growth rate for any given real frequency. The Briggs-Bers criterion can thus be applied in this case.

To determinate if a possible unstable mode is an instability, the trajectory of its wavenumber in the complex k-plane is recorded as $\omega = \mathrm{Re}\,(\omega) + \mathrm{i}\,\mathrm{Im}\,(\omega)$ is varied. More specifically, $\mathrm{Re}\,(\omega)$ is fixed while $\mathrm{Im}\,(\omega)$ is varied from $-\infty$ to 0. Fig. 7 shows this process for $\mathrm{Re}(\omega) = 0.9271$, while the imaginary part $\mathrm{Im}\,(\omega)$ goes from -1.4 to 0. The wavenumber of the possible unstable mode crosses the real k-axis from the lower k-plane when $\mathrm{Im}\,(\omega)$ is approaching 0. The crossing of the real k-axis from the lower half k-plane indicates that this mode is indeed a downstream propagating mode and is thus an instability.

In addition, in order to discard the existence of an absolute instability, it should be verified, that the trajectories of the wavenumbers in the k-plane for any $\mathrm{Re}\,(\omega)$ do not show any saddle point, which corresponds to merging roots of k from different halves of the k-plane. This has been carefully checked on a large range of values of $\mathrm{Re}\,(\omega)$. To sum up, for $\omega = 0.9271$, there is only one hydrodynamic instability, and it is a convective instability.

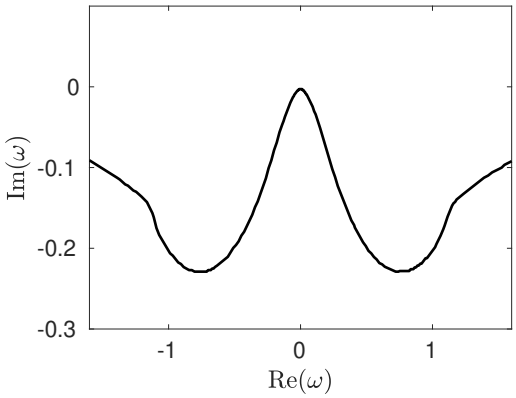

Fig. 6. Growth rate of the unstable mode for a real wavenumber and for $M = 0.3$.

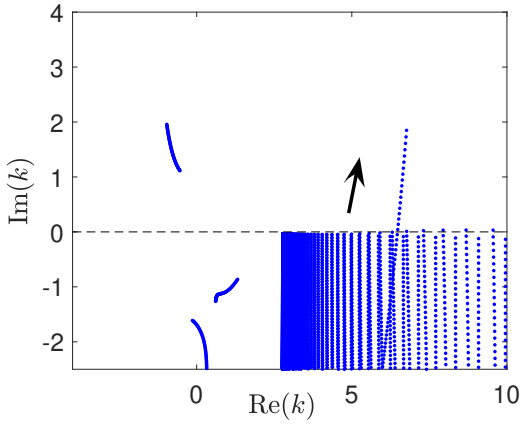

Fig. 7. Trajectories of the wavenumbers for $\mathrm{Re}\,(\omega) = 0.9271$ as $\mathrm{Im}\,(\omega)$ varies from -1.4 to 0. The arrow indicates the direction of increasing $\mathrm{Im}\,(\omega)$.

3.3. Characterization of the instability from time-domain simulation

3.3.1. Instability type

The type of the instability observed in the time-domain simulations can also be investigated by considering acoustic propagation driven by a harmonic source with $\omega = 0.9271$. The logarithm of $|p|$ on the lined wall $z = 1$ varying with t and x is shown in Fig. 8. With a harmonic source, the response of pressure has a constant value at $x = 0$. The attenuation by the liner can be noticed along the upstream direction, and the hydrodynamic instability is observed in the downstream direction. Once a steady-state is attained, the magnitude of the instability at a given location is not increasing over time. It thus appears that the instability observed in the time-domain simulation is also a convective one.

3.3.2. Wavenumber

If the instability is convective and is the main contribution to the pressure field, the fluctuating pressure will have the form:

$$p\,(x, z, t) = P_{\mathrm{HI}}\,(z)\,\mathrm{e}^{\mathrm{i}\omega t}\mathrm{e}^{-\mathrm{iRe}(k_{\mathrm{HI}})x}\mathrm{e}^{\mathrm{Im}(k_{\mathrm{HI}})x}, \tag{14}$$

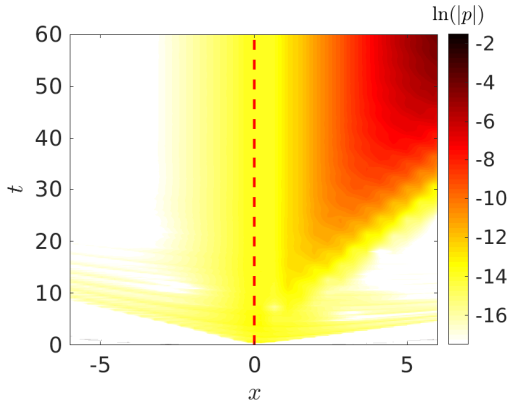

Fig. 8. Pressure response $\ln|p(x, z = 1, t)|$ to a harmonic source at $\omega = 0.9271$ obtained from the time-domain simulation for $M = 0.3$. The source position is indicated by the vertical dashed line.

where P_{HI} is the mode shape of the instability and k_{HI} is its wavenumber.

In this case, the phase of the complex pressure, denoted by arg is given by:

$$\arg[p(x, z, t)] = -\mathrm{Re}(k_{\mathrm{HI}})\, x + \omega t + \arg[P_{\mathrm{HI}}(z)]. \tag{15}$$

The real part of the instability wavenumber can then be estimated from the time-domain solution through the axial evolution of the phase of the complex pressure. Fig. 9 shows $\arg(p)$ along the liner ($z = 1$) at $t = 90$, for which it has been checked that the instability is well developed. The phase has been unwrapped to ensure that $\arg(p)$ is continuous. The estimated slope for $2 \leq x \leq 6$ of the phase is -6.89, which is very close to the prediction of modal analysis $\mathrm{Re}(k_{\mathrm{HI}}) = 6.78$.

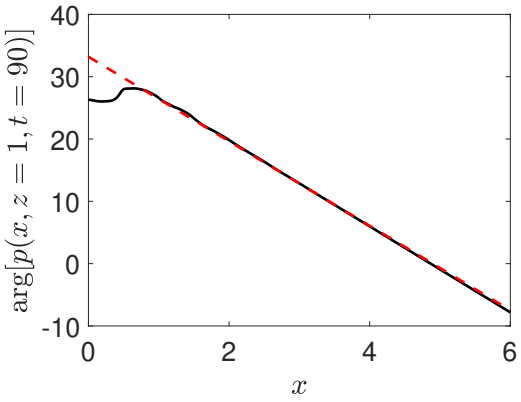

Fig. 9. Comparison of the phase of the pressure on the lined wall from the time-domain solution at $t = 90$ ——— and from the analytical solution in Eq. (15) ($\arg(p) \propto -6.78x$) - - - - .

Similarly, the growth rate of the convective instability $\mathrm{Im}(k_{\mathrm{HI}})$ in Eq. (14) can be calculated from the logarithm of $|p(x, z, t)|$:

$$\ln|p(x, z, t)| = \mathrm{Im}(k_{\mathrm{HI}})\, x + \ln|P_{\mathrm{HI}}(z)|. \tag{16}$$

A snapshot of $\ln|p|$ at $t = 90$ from the time-domain simulation is depicted in Fig. 10 (a). The

instability is seen growing from the source at the vicinity of the liner. Fig. 10 (b) shows the spatial variation of $\ln|p(x, z = 1, t = 90)|$. A linear growth is observed downstream, where the instability is the dominant contribution to the pressure field. The estimated slope for $2 \leq x \leq 6$ is 1.99, which is again in close agreement with the spatial growth rate predicted by modal analysis $\mathrm{Im}\,(k_{\mathrm{HI}}) = 1.97$.

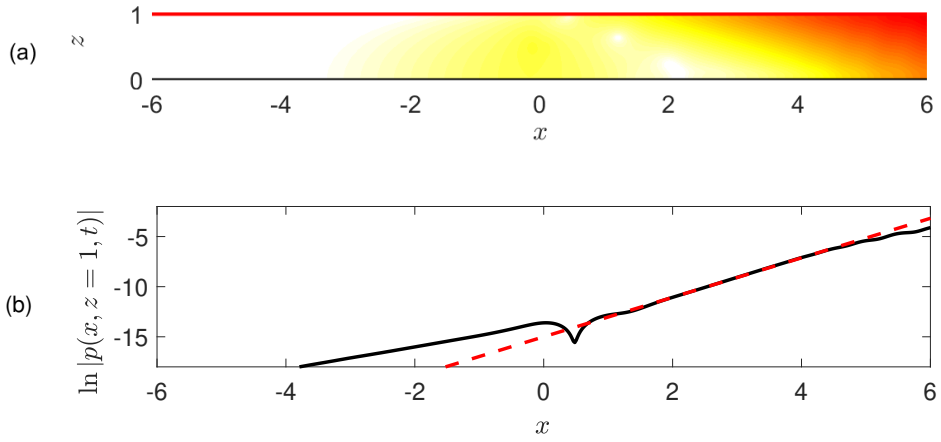

Fig. 10. (a) Snapshot of $\ln|p|$ at $t = 90$ and (b) comparison of the amplitude of the pressure on the lined wall from the time-domain solution ——— and from the analytical solution in Eq. (16) ($\ln|p| \propto 1.97x$) - - - - .

Another example for a different frequency $\omega = 0.4636$ can be found in Appendix B. This shows the viability of the time-domain method in simulating the instability.

3.3.3. Mode shapes

The mode shapes P, U and V of the instability determined from modal analysis are compared with the vertical profiles of p, u and v calculated from the time-domain solution in Fig. 11. The results of the time-domain solution correspond to the section $x = 4$ at $t = 90$, for which it has been checked that the solution is not changing after additional time iterations. When the time-domain solution is in a steady-state, the vertical profiles of p, u and v should hold similar shapes regardless of x-position and time iteration. For comparison, the mode shapes of the instability and the vertical profiles of p, u and v are normalized by the maximum of the pressure modulus. The peaks of the amplitudes are observed near the lined wall. Then they gradually decrease to a small value on the rigid wall. The match between modal analysis and the time-domain solution is remarkable.

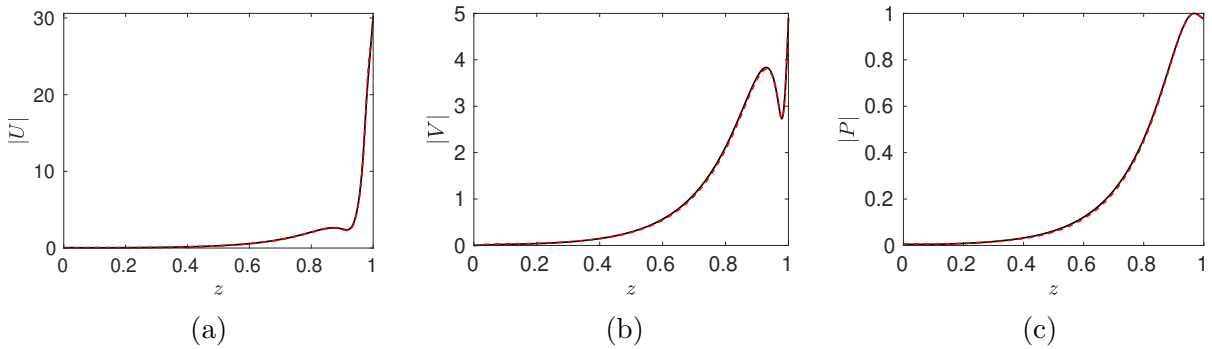

Fig. 11. Comparison of the mode shape of the instability for (a) $U(z)$, (b) $V(z)$ and (c) $P(z)$ ——— determined from the time-domain solution at $x = 4$ and $t = 90$ and - - - - calculated by modal analysis.

4. Convergence of instability

Previous studies on the same topic, i.e., instabilities appearing during sound propagation in a lined flow duct, have investigated the impact of spatial filters and grid resolution on the instabilities. It was concluded that selective filtering is effective to remove or partly remove the instability [34, 3] and that the use of fine grids can reinforce the instability [27, 2], in particular when using the Myers impedance boundary condition instead of resolving the boundary layer as done here. Therefore, the effects of both factors on the hydrodynamic instabilities are studied.

4.1. Effect of the filtering strength

In the time-domain simulations, a selective filter of strength σ is applied on the whole domain to remove the grid-to-grid oscillations. In the previous sections, σ was set to 0.5. Simulations are now performed with different values of σ in order to study how the properties of the hydrodynamic instability are modified.

Fig. 12 shows the real and imaginary parts of the instability wavenumber obtained with the time-domain solutions as a function of σ. The results are compared with the reference wavenumber obtained by modal analysis. When the strength of selective filter is between 0.7 and 1, the strong dissipation of the selective filter results in a noticeable deviation between the reference result and the time-domain prediction. In particular, the growth rate of the instability is overestimated. As σ decreases, $\mathrm{Re}(k_{\mathrm{HI}})$ and $\mathrm{Im}(k_{\mathrm{HI}})$ start to approach the reference wavenumber. The value of σ does not make a significant difference to $\mathrm{Re}(k_{\mathrm{HI}})$ and $\mathrm{Im}(k_{\mathrm{HI}})$, when it is in the range between 0.2 and 0.5. For σ below 0.2, spurious numerical waves with a short wavelength are rapidly growing near the duct walls and the simulations become unstable instantly. Therefore, for accurately predicting the hydrodynamic instability, the filtering strength should be chosen as small as possible while sufficiently large to stabilize the numerical calculation. A value of σ between 0.2 and 0.5 seems to be a good compromise considering the time step used in the time-domain simulations.

4.2. Effect of the mesh size along the duct height

Along the x-direction, centered high-order finite-difference schemes, with dispersion-relation preserving properties, are employed. It is assumed that the mesh size Δx is small enough so that the dispersion properties of the instability are well-reproduced. In particular, it has been checked

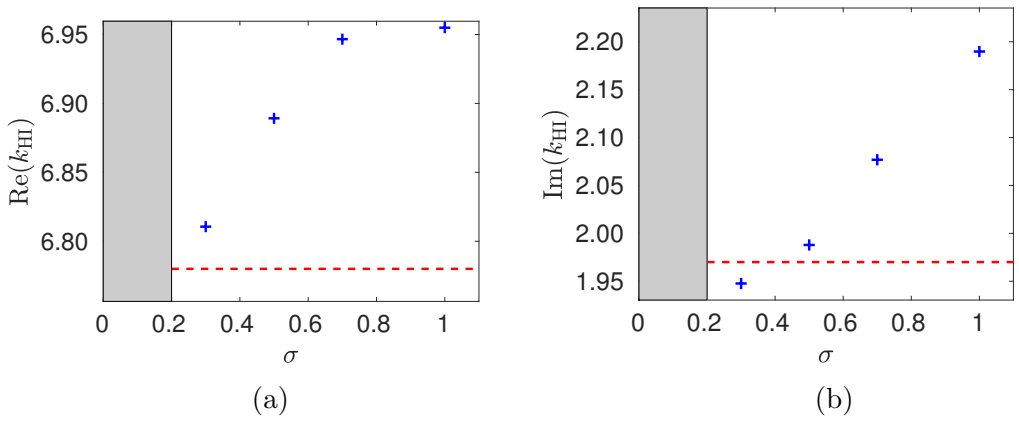

Fig. 12. (a) Real and (b) imaginary parts of the instability wavenumber + estimated from the time-domain solution as a function of the filtering strength σ and - - - predicted by modal analysis. The grey region indicates unstable simulations.

that $k^*(k_{\mathrm{HI}})$ is very close to k_{HI}, where k^* is the effective wavenumber of the centered finite-difference scheme employed here. No particular effect in reducing Δx is thus expected. The grid along the z-direction is anticipated to have more impact on the instability. Indeed, non-centered schemes are used near the walls, which enhance dispersion. They can amplify or dissipate even constant-amplitude waves, contrary to centered schemes. In addition, the instability is directly related to the mean flow profile through u_0 and $\mathrm{d}u_0/\mathrm{d}z$. The discretization of the mean flow profile, in particular within the boundary layer, is expected to play a role in the results.

Fig. 13 shows the impact of the number of grid points along the z-direction n_z on the real and imaginary parts of the instability wavenumber. For $n_z \leq 155$, the deviations of $\mathrm{Re}(k_{\mathrm{HI}})$ and $\mathrm{Im}(k_{\mathrm{HI}})$ estimated from the time-domain simulations and the modal analysis are noticeable. Note that the mesh is already fine enough for $n_z = 55$ to precisely calculate the acoustic propagation. As shown in [57], the pressure of instabilities should decay exponentially away from the lining as $\exp[-\mathrm{Re}(\mu)(1-z)]$ with $\mu^2 = k^2 - (\omega - Mk)^2$. In the present case, $\mathrm{Re}(\mu) = 6.69$ so that the number of points per wavelength is about $2\pi n_z/\mathrm{Re}(\mu) \approx 52$, which is very large. However, that is still not sufficient to precisely calculate the hydrodynamic instability. As n_z increases, the features of hydrodynamic instability can be captured and the wavenumber gradually approaches the prediction of modal analysis. With $n_z \geq 175$ the time-domain solution is deemed converged.

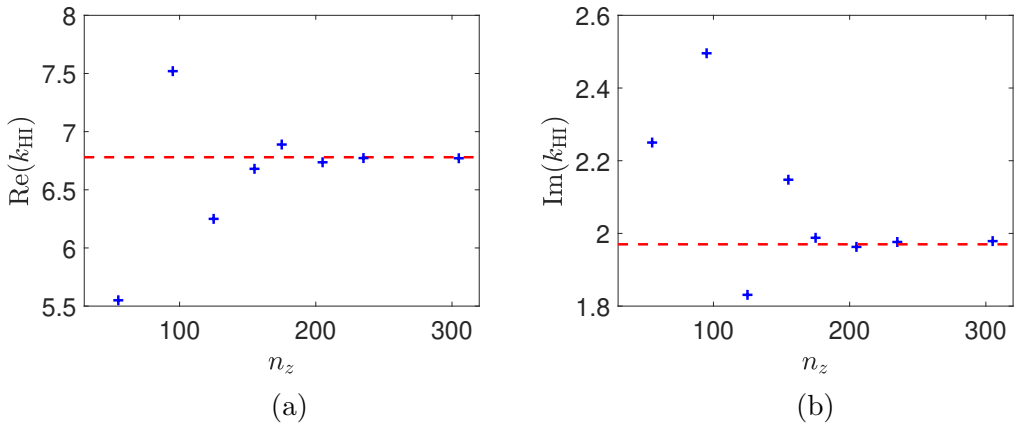

Fig. 13. (a) Real and (b) imaginary parts of the instability wavenumber + estimated from the time-domain solution as a function of the number of grid points along the duct height n_z and - - - predicted by modal analysis.

5. Suppression of the hydrodynamic instability

In all cases tested with realistic Mach numbers, it was not possible to prevent the appearance of the instability using coarse grids and increased selective filter strength. We turned therefore to the methods based on the stabilization via modification of the underlying equations. Given the similar performance of many of these methods in turbulent jets [44], we opted for the gradient term suppression (GTS) method due to its simplicity and performance.

In the case that the acoustic field is generated by an impulsive source, as in the present case, it may be possible to separate the acoustic and instability components in time through a temporal window. This would allow to account for the full LEE, but it is of use only when the instability is weak enough. In general, a robust suppression strategy is needed with a minimal impact on acoustic propagation.

5.1. Partial GTS

A natural generalization of the original GTS method is used here to suppress the instability, consisting of a partial suppression of the gradient term instead of a complete suppression. Eqs. (1) are modified by adding a coefficient ϵ in front of the term of $\mathrm{d}u_0/\mathrm{d}z$. Therefore, Eq. (1b) turns to

$$\frac{\partial u}{\partial t} + u_0 \frac{\partial u}{\partial x} + \epsilon \frac{\mathrm{d}u_0}{\mathrm{d}z} v + \frac{\partial p}{\partial x} = 0 \tag{17}$$

where ϵ adjusts the strength of the mean flow gradient term and ranges from 1 to 0.

Combining Eqs. (1a), (17) and (1c) leads to the wave equation:

$$\frac{\mathrm{D}}{\mathrm{D}t}\left(\frac{\mathrm{D}^2 p}{\mathrm{D}t^2} - \nabla^2 p\right) + (\epsilon + 1)\frac{\mathrm{d}u_0}{\mathrm{d}z}\frac{\partial^2 p}{\partial x \partial z} = \frac{\mathrm{D}^2 Q}{\mathrm{D}t^2} \tag{18}$$

where $\mathrm{D}/\mathrm{D}t = \partial/\partial t + u_0\,\partial/\partial x$ is the material derivative. In particular, the Lilley's equation is recovered for $\epsilon = 1$. The decrease of ϵ from 1 to 0 is thus equivalent to transforming the original Lilley's equation, which sustains unstable modes, to a simplified form of Lilley's equation which appears to be inherently stable [35]. In addition, decreasing ϵ from 1 to 0 diminishes the

refraction term proportional to $\mathrm{d}u_0/\mathrm{d}z$ in the original Lilley's equation by a factor of two. A gradual suppression of the instability is then expected when diminishing the value of ϵ.

Another remarkable value is $\epsilon = -1$ for which Eq. (18) corresponds to the material derivative of the convected wave equation. However, Eq. (18) is already stable for $\epsilon = 0$. In addition, it will be shown that the prediction of the acoustic propagation tends to be deteriorated with the decrease of ϵ. Therefore, the study is hereafter restricted to $\epsilon \in [0, 1]$.

The GTS method is expected to provide an accurate prediction of acoustic propagation at high frequencies [35]. This can be explained by conducting an order of magnitude analysis. The order of the magnitude of each term in Eq. (1b) is as follows:

$$\frac{\mathrm{D}u}{\mathrm{D}t} \sim (\omega - Mk)\hat{u}, \qquad \frac{\mathrm{d}u_0}{\mathrm{d}z}v \sim \frac{M}{\delta}\hat{v}, \qquad \frac{\partial p}{\partial x} \sim k\hat{p},$$

where for acoustic modes the wavenumber is in the order of the frequency $k \sim \omega$ and the acoustic variables are in the same order of magnitude $\hat{u} \sim \hat{v} \sim \hat{p}$. The mean flow gradient term in Eq. (1b) can be neglected if

$$\left| v\frac{\mathrm{d}u_0}{\mathrm{d}z} \right| \ll \left| \frac{\partial p}{\partial x} \right|, \left| \frac{\mathrm{D}u}{\mathrm{D}t} \right|. \tag{19}$$

which, considering the orders of magnitude above, shows that the mean flow gradient term is expected to have a negligible effect on the acoustic propagation for $\omega\delta \gg M$. This explains why the high frequency components are less impacted by the partial GTS method.

5.2. Effect on the wavenumber and the mode shape

The wavenumbers are studied when ϵ varies from 1 to 0. Fig. 14 shows the wavenumbers in the k-plane determined by modal analysis for different values of ϵ for the rigid and partially lined duct. It is first noticed that modifying ϵ tends to move all the modes in the complex k-plane. The instability for the lined duct, observed for $\epsilon = 1$, is not seen for the smaller values of ϵ, which shows that a small decrease of ϵ is sufficient to suppress the instability. Also, the wavenumbers for the rigid duct are less sensitive to ϵ than for the lined duct.

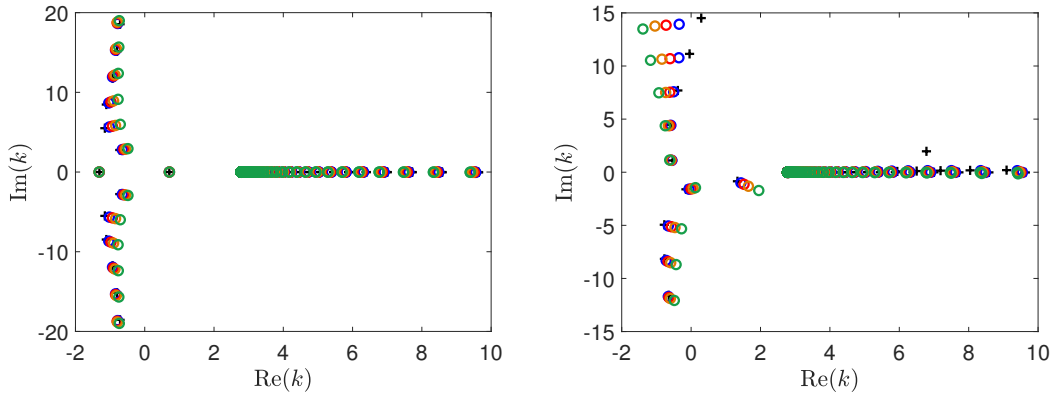

Fig. 14. Wavenumbers in the k-plane at $\omega = 0.9271$ for a duct (a) with two rigid walls, (b) with one rigid wall and for different strengths of gradient term: + $\epsilon = 1$, ○ $\epsilon = 0.7$, ○ $\epsilon = 0.5$, ○ $\epsilon = 0.3$ and ○ $\epsilon = 0$.

To analyze more finely the effect of ϵ on the instability, the variations of the instability wavenumber are plotted as a function of ϵ in Fig. 15. The results are shown for three different grid sizes ($N = 100$, 200 and 300). The growth rate of the unstable mode $\mathrm{Im}(k_{\mathrm{HI}})$ decreases gradually with ϵ which proves the stabilizing effect of decreasing ϵ. It is interesting to note that for $\epsilon \leq 0.94$, the wavenumber of the unstable mode starts depending on the grid size. There, the unstable mode merges into the continuous spectrum of convected modes near the real k-axis.

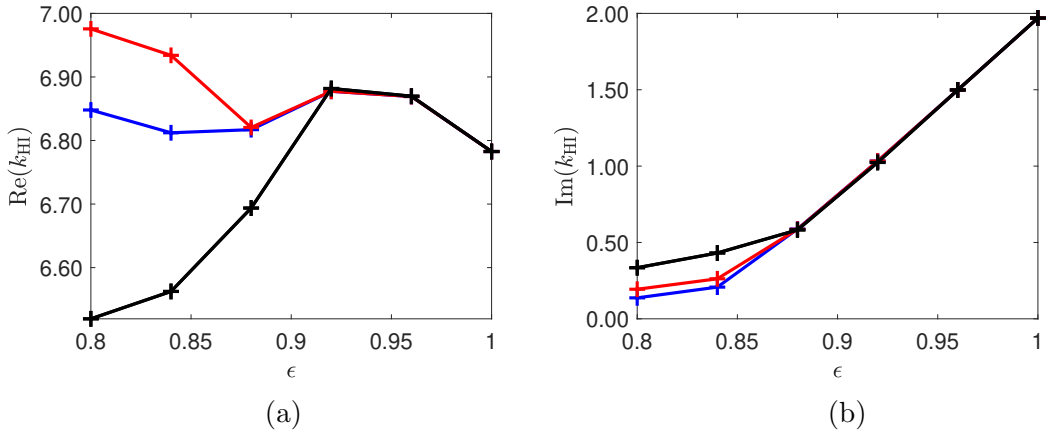

Fig. 15. Variations of the (a) real and (b) imaginary parts of the instability wavenumber k_{HI} as a function of ϵ for different numbers of grid points: $N = 100$, $N = 200$ and $N = 300$.

Acoustic modes are also affected by reducing the parameter ϵ. To quantify the impact of the partial GTS method on the wavenumbers of the acoustic modes, the attenuation rate of the propagative acoustic mode is provided in Fig. 16 (a). The attenuation rate α, defined as $\alpha = 20 \log_{10} \mathrm{e}^{-\mathrm{Im(k)}}$, expresses the decrease per unit distance (H) of the signal amplitude during the propagation along the axial direction. For $\omega = 0.9271$, the attenuation rate of the plane wave mode increases from 7.39 to 14.95 dB/H when ϵ decreases from 1 to 0.

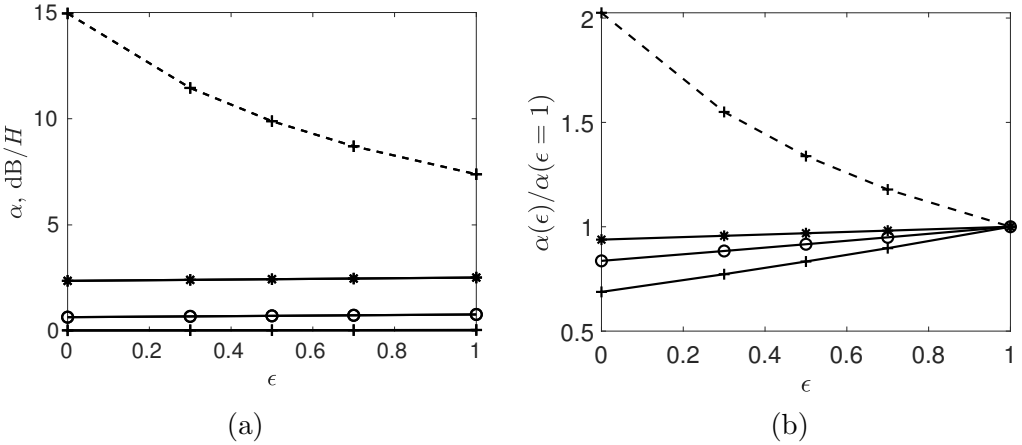

Fig. 16. (a) Attenuation rate of acoustic modes and (b) ratio of the attenuation rate determined for the partial GTS method to that for the original LEE for (dashed) $\omega = 0.9271$ and (full) $\omega = 9.271$: + plane wave mode, $\circ$ second downstream propagative mode and $*$ third downstream propagative mode.

In addition, Fig. 17 depicts the mode shapes of the acoustic velocity components and pressure for the plane wave mode and for the leading upstream and downstream evanescent modes for different values of ϵ. The modulus of all three variables are normalized by the maximum of $|P|$. Modifying ϵ has an evident impact on $|U|$ and $|V|$, noticeably near the lined wall. This effect is particularly dramatic for $|U|$, whose peak on the lined wall decreases by a factor of 10 from $\epsilon = 1$ to $\epsilon = 0$. Also, a noticeable increase of $|V|$ near the lined wall is observed as ϵ decreases. Concerning the pressure, the mode shape does not vary too much with ϵ. For the plane wave mode, a decrease of the amplitude is noticed near the rigid wall, while for the evanescent modes, the amplitude grows gradually near the lined wall as ϵ decreases.

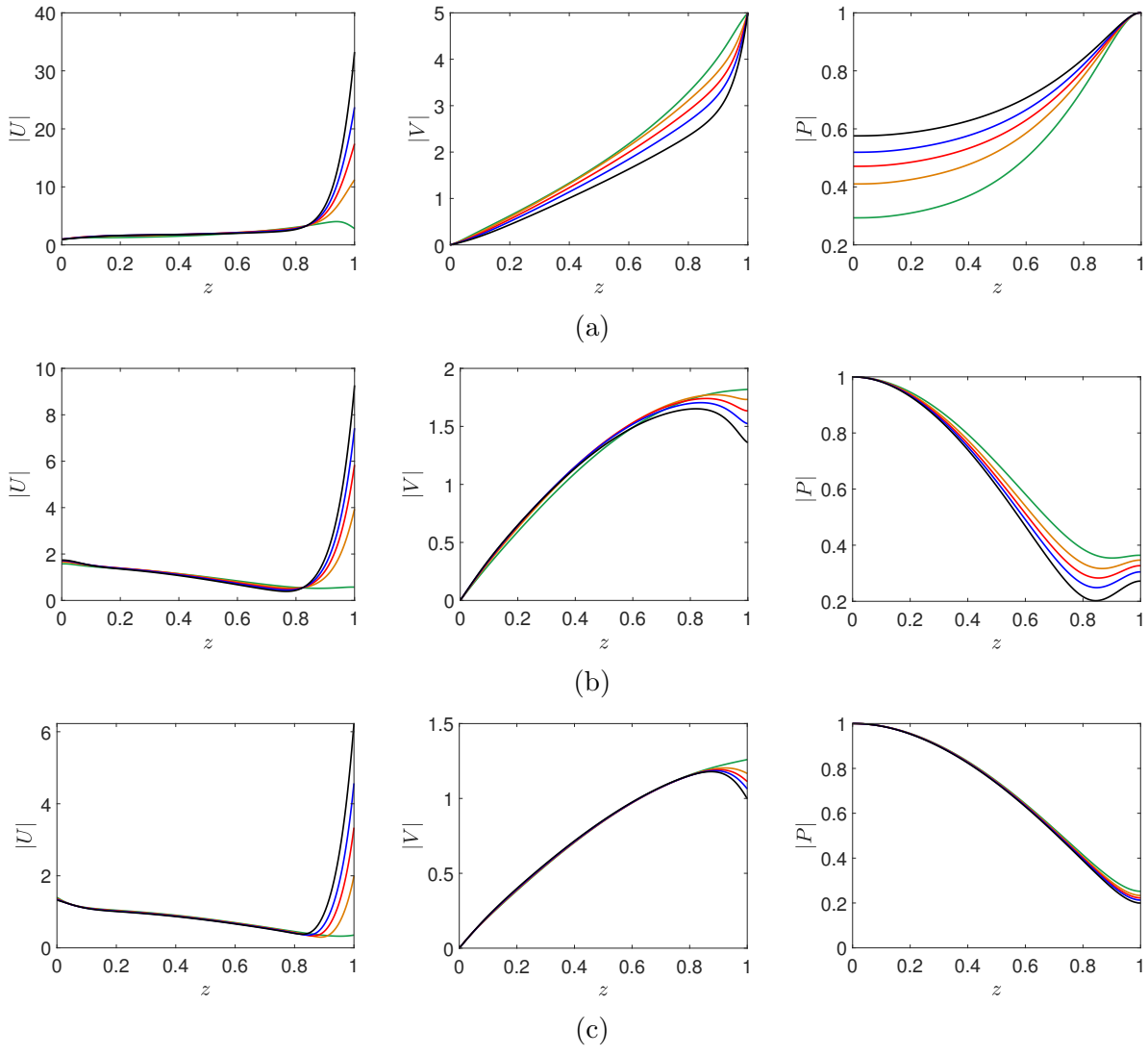

Fig. 17. Mode shapes for the MSD liner at $\omega = 0.9271$ and for several values of ϵ: (a) plane wave mode and leading (b) downstream and (c) upstream evanescent modes for, from left to right, velocity components along x and z-direction and pressure: $\epsilon = 1$, $\epsilon = 0.7$, $\epsilon = 0.5$, $\epsilon = 0.3$ and $\epsilon = 0$.

The impact of the partial GTS method on the acoustic propagation at high Helmholtz numbers

is here studied. Fig. 18 provides the mode wavenumbers for $\omega = 9.271$, while keeping the same impedance and boundary layer thickness as for $\omega = 0.9271$. Three downstream propagative modes are noticed and no unstable mode is observed. The mode wavenumbers are less changed due to the partial GTS method compared with Fig. 14. The attenuation rates for the three downstream propagative modes are also plotted in Fig. 16 (a). The deviation caused by the gradient term suppression are respectively 0.017, 0.13 and 0.16 dB/H for the three modes. The ratio of the attenuation rate obtained with the partial GTS method to that determined with the original LEE is also shown in Fig. 16 (b). It is seen that the largest changes of attenuation rate occur for low Helmholtz numbers.

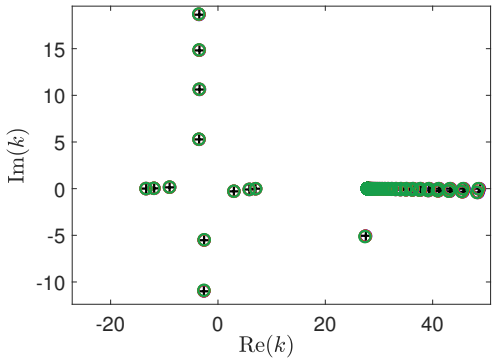

Fig. 18. Wavenumbers in the k-plane at $\omega = 9.271$ for a lined duct and for several values of ϵ: + $\epsilon = 1$, ○ $\epsilon = 0.7$, ○ $\epsilon = 0.5$, ○ $\epsilon = 0.3$ and ○ $\epsilon = 0$.

5.3. NASA GIT benchmark

The GTS method is now applied to the GIT benchmark problem [58], which is widely used for validation of aeroacoustic solvers of lined ducts under plane wave propagation. A number of numerical studies have reported the existence of an instability at 1 kHz for this problem [16, 59, 28]. The tube has a dimension of $0.8128 \times 0.0508 \times 0.0508$ m. The upper wall is lined with a ceramic tubular liner (CT57) with a length of 0.406 m. The sound pressure level (SPL) and phase of acoustic waves have been measured at various Mach numbers and for frequencies from 500 Hz to 3 kHz.

The source is installed ahead of the section $x = 0$ at a distance of 0.05 m. The mean velocity profile is given by Eq. (2), with a Mach number of 0.335 and a boundary layer thickness equal to 2 % of the duct height. A grid of 55 points is used along the z-direction, while the grid size along the x-direction is $\Delta x = 0.0011$ m. The time step has been set to 2×10^{-6} s. The broadband admittance of the liner (see. Eq. (6)) is obtained by a fit of the educed values provided by Jones *et al.* [58] for $M = 0.335$. In this case, two pairs of complex-conjugate poles are sufficient to have a good match from 500 Hz up to 3 kHz, as shown in Fig. 19. The coefficients of the obtained admittance model are given in Table 1.

Fig. 20 shows a series of successive snapshots of the pressure. The left and right columns correspond to the results without GTS ($\epsilon = 1$) and full GTS ($\epsilon = 0$), respectively. We focus first on the case without GTS. Once the incoming pulse encounters the liner leading edge, it splits into two wave fronts, a first one that is transmitted downstream and is progressively attenuated by the liner, and a second one that is reflected upstream. At the same time, the instability is generated

Table 1: Coefficients of the rational function for the normalized broadband admittance model of CT57

	α_i	β_i	B_i	C_i	Y_∞
$i=1$	6135	−14886	−4584	3729	1.16
$i=2$	507	5577	1788	−290	

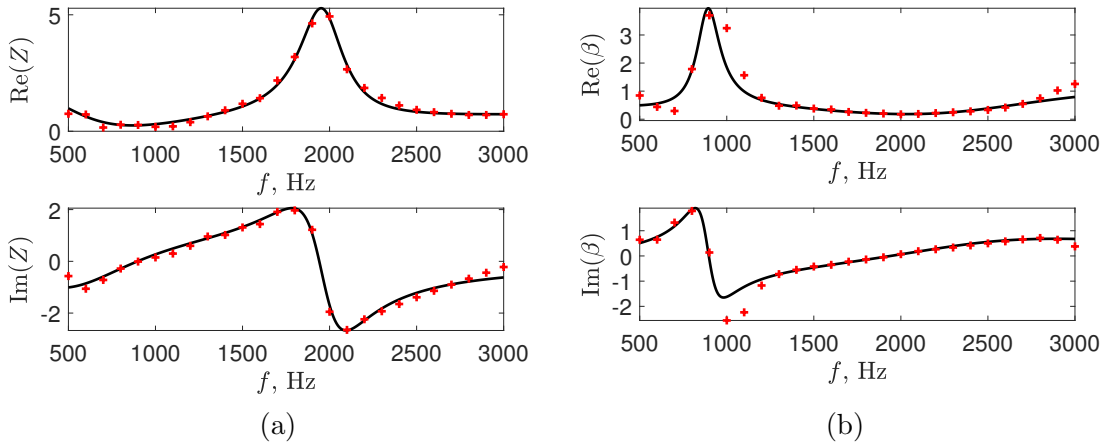

Fig. 19. (a) Impedance and (b) admittance of the CT57 liner: + NASA educed values and ——— fit obtained with the vector fitting algorithm.

at the leading edge of the liner. Briefly afterwards, when most of the transmitted and reflected acoustic pulses have left the computational domain, the instability takes over in the entire lined section, leading to a divergent pressure field. In the case of full GTS, the same overall behavior is observed for the acoustic component. However, no instability is generated and the acoustic energy falls to zero at increasing times.

Even though the full GTS method shows encouraging results for suppressing instabilities, it should be applied carefully. Indeed, it may not be always physically valid to ignore the instability. Alomar *et al.* [9] showed experimentally a feedback mechanism between the instability and the acoustic waves for a liner of finite length. The instabilities generated at the leading edge of the liner are scattered into acoustic waves at the trailing edge; these acoustic waves propagate upstream and trigger another instabilities once they are scattered at the leading edge. This feedback mechanism can not be reproduced when the full GTS method is employed.

The time series of the pressure at three virtual microphones located on the rigid wall, at different axial locations, are shown in Fig. 21 for several values of ϵ. The successive appearance of the initial acoustic pulse and the instability is observed at all three locations. The impact of ϵ is mainly on the instability component: decreasing values of ϵ induces a delay in the emergence of the instability. This is the expected behavior, as decreasing ϵ causes a decrease of the amplification of the unstable mode, and thus it takes more time for the instability to leverage the acoustic pressure levels. For $\epsilon = 0.3$ and 0, no instability appears within the simulation time.

In order to obtain the frequency spectrum of the pressure field, a tapered cosine window is applied to the pressure signals to discard the instability component, as shown in Fig. 22. The Fourier transform of the filtered signals is then computed. Note that for the cases for which the partial GTS method induces a delay in the appearance of the instability, the window could have

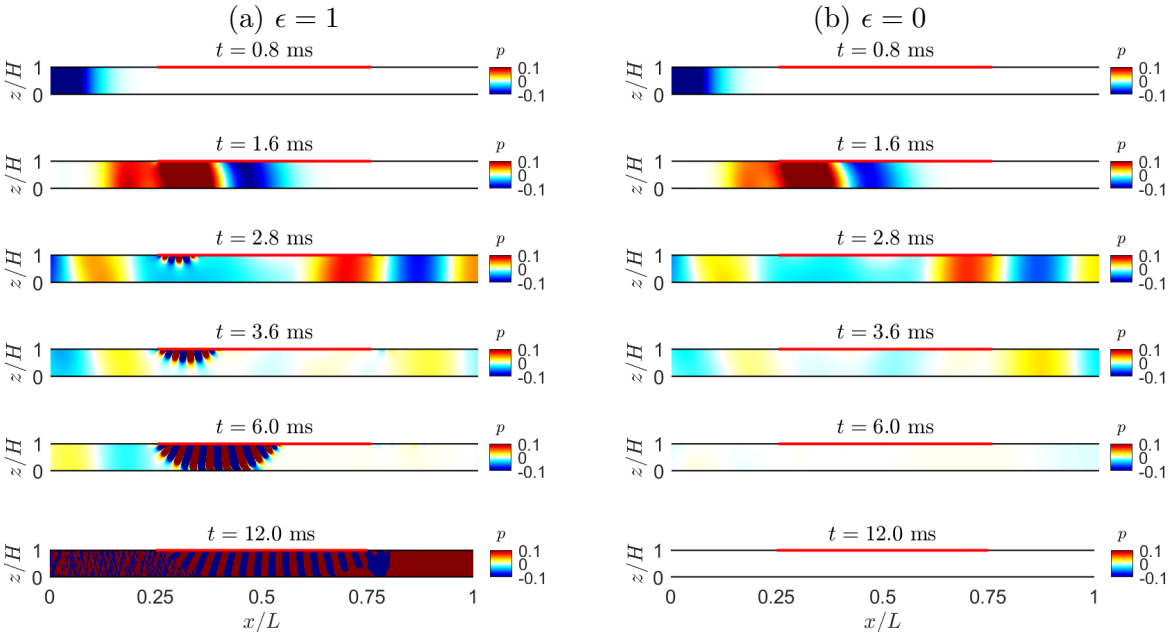

Fig. 20. Pressure map (Pa) along the duct at different times for (a) $\epsilon = 1$ and (b) $\epsilon = 0$.

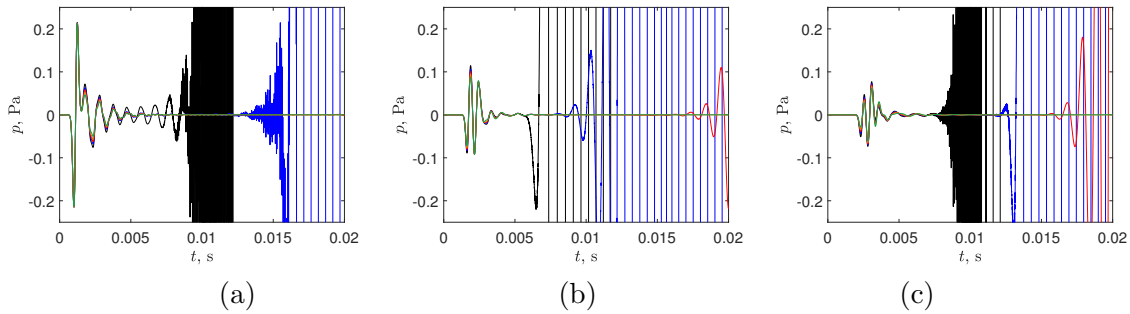

Fig. 21. Time series of pressure on the rigid wall at (a) $x = 0.12\,L$, (b) $x = 0.5\,L$ and (c) $x = 0.86\,L$ for: $\epsilon = 1$, $\epsilon = 0.7$, $\epsilon = 0.5$, $\epsilon = 0.3$ and $\epsilon = 0$.

be chosen longer; moreover, for the cases for which the partial GTS allows a suppression of the instability, the window is not necessary. However, for consistency, the same window is applied on all the pressure signals and for all the cases considered.

The resulting SPL and phase of the acoustic pressure along the duct wall opposite to the liner are shown in Fig. 23, at different frequencies and for different values of ϵ. For comparison with the NASA measurements, the curves are adjusted so that the SPL and the phase are 130 dB and 0°, respectively, at $x = 0$. Without GTS ($\epsilon = 1$), some oscillations on the SPL and on the phase are observed at 500, 1000 and 1500 Hz in the lined section. These are due to the difficulty in isolating the acoustic contribution by simple windowing. Indeed, as seen in Fig. 21 (a) and (b), there is an overlap near $t = 0.005$ s between the acoustic pulse and the instability. An obvious deviation between the simulations and the experimental results is noticed at 3 kHz. One of the reasons is that the window function applied for calculating the Fourier transform does not account for the full acoustic signal. It can also be partly explained by the proximity of the cut-off frequency of the rigid duct, which

induced a significant error in the impedance eduction of the liner in the GIT experiment. Overall, the trends of both the SPL and the phase are insensitive to ϵ. Decreasing ϵ tends to underestimate the pressure levels, especially downstream of the liner. The largest discrepancies are observed at $f = 1$ and 3 kHz. For the other frequencies, the SPL predictions are within a few dBs from the measured values.

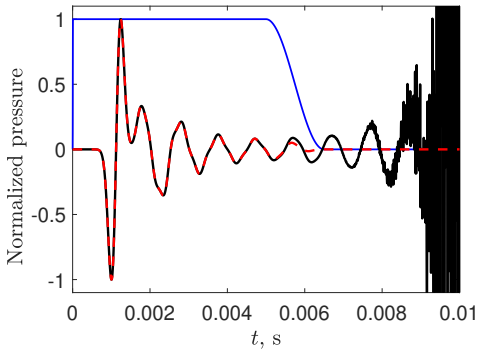

Fig. 22. Window function used for signal processing ——— and example of (normalized) pressure signal at $x = 0.12\,L$ before ——— and after windowing - - - -.

To assess the effectiveness of the GTS, another quantity of interest, namely the insertion loss (IL), is considered. It is defined as the difference in acoustic power at the exit section $x = L$ with and without liner. Details on the calculation of the acoustic power from the time-domain numerical solution can be found in Troian *et al.* [50]. Fig. 24 shows the frequency variations of IL calculated for different values of ϵ, as well as estimated from the NASA measurements. A peak is observed close to the liner resonance (1.1 kHz) for $\epsilon = 1$ and 0.7, in good agreement with the experimental values. The impact of ϵ on the IL is weak except in the immediate vicinity of the resonance and also for $f > 2.5$ kHz. Note that even if a significant increase of IL is observed for $f > 2.5$ kHz when decreasing ϵ, a good match is achieved for $\epsilon = 0.5$. Figs. 21 and 23 show that, for this particular case, $\epsilon = 0.5$ seems to be the optimal value ensuring a good compromise between stable simulation and accurate prediction. However, this is not a general conclusion, as the optimal value of ϵ may depend on the flow profile, the Mach number and the liner, among others, and may thus be different from case to case.

The NASA GIT benchmark deals with small Helmholtz numbers ($\omega \leq 2.8$). To examine the performance of the partial GTS method for high Helmholtz numbers, an additional set of time-domain simulations are conducted for a duct whose height $H = 0.508$ m is 10 times larger than the one of the NASA GIT duct. The lengths of the duct and of the liner are also increased, with respective values of 4.06 m and 2.03 m. The boundary layer thickness of the mean flow remains equal to 2 % of the duct height. The numerical parameters are the same as before except the number of grid points along the z-direction, set to $n_z = 175$.

The time series of the pressure at $x = 0.5\,L$ on the rigid wall of the large duct are presented for several values of ϵ in Fig. 25. Compared with the waveforms for the smaller duct in Fig. 21, the signals are more complex because of the multimodal propagation. Instabilities are only observed for $\epsilon = 1$ and do not appear when the partial GTS method is applied. A view on the pressure response for 0.004 s $< t <$ 0.01 s is shown in Fig. 25 (b). The signals for the several values of ϵ are almost superimposed even if the amplitude of the waveform is slightly reduced as ϵ decreases.

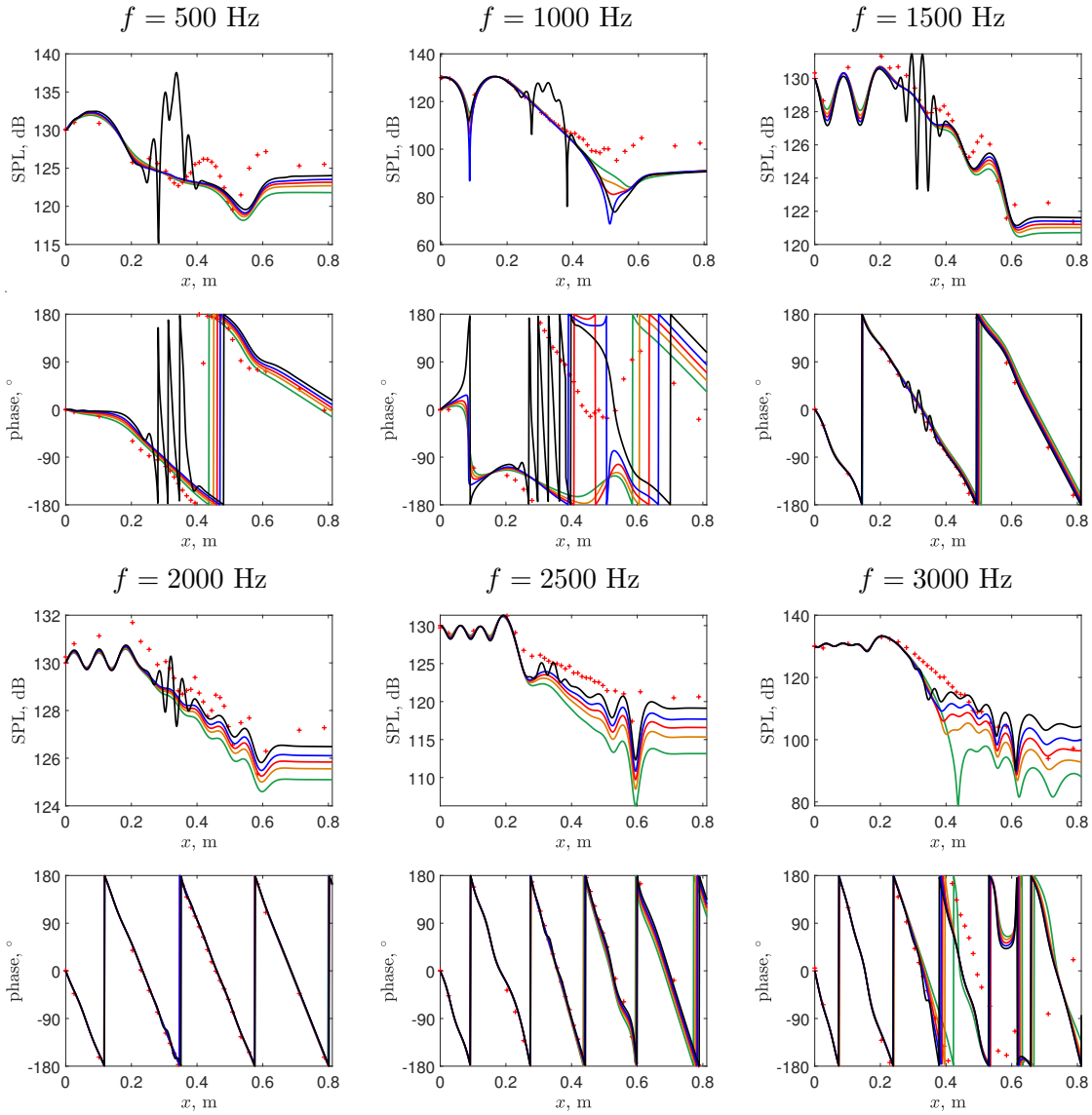

Fig. 23. SPL and phase of the acoustic pressure along the duct for $M = 0.335$ and for different values of ϵ: $\epsilon = 1$, $\epsilon = 0.7$, $\epsilon = 0.5$, $\epsilon = 0.3$, $\epsilon = 0$, + NASA experiments.

The SPL and phase along the large duct on the wall opposite to the liner are provided for three frequencies and for several values of ϵ in Fig. 26. A window function, shown in Fig. 25 (a) is also applied to avoid the influence of instabilities and is wider than the one shown in Fig. 22. Compared with the results for the NASA GIT duct shown in Fig. 23, the differences due to the suppression of the gradient term are relatively small.

Finally, the powers W at the exit plane $x = L$ are compared for several values of ϵ and for both ducts. Fig. 27 shows the power difference ΔW, which is defined as $\Delta W = 10 \log_{10}[W(\epsilon)/W(\epsilon = 1)]$, where $W(\epsilon)$ is the power when the partial GTS method is applied and $W(\epsilon = 1)$ is the power calculated from the original LEE solution. For the NASA GIT case, ΔW has a large peak near $f = 1.1$ kHz due to the suppression of the instability and has largest variations near $f = 3$ kHz.

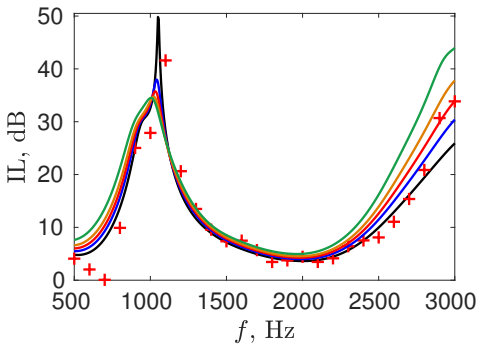

Fig. 24. Insertion loss for $M = 0.335$ and for: $\epsilon = 1$, $\epsilon = 0.7$, $\epsilon = 0.5$, $\epsilon = 0.3$, $\epsilon = 0$, + NASA experiments.

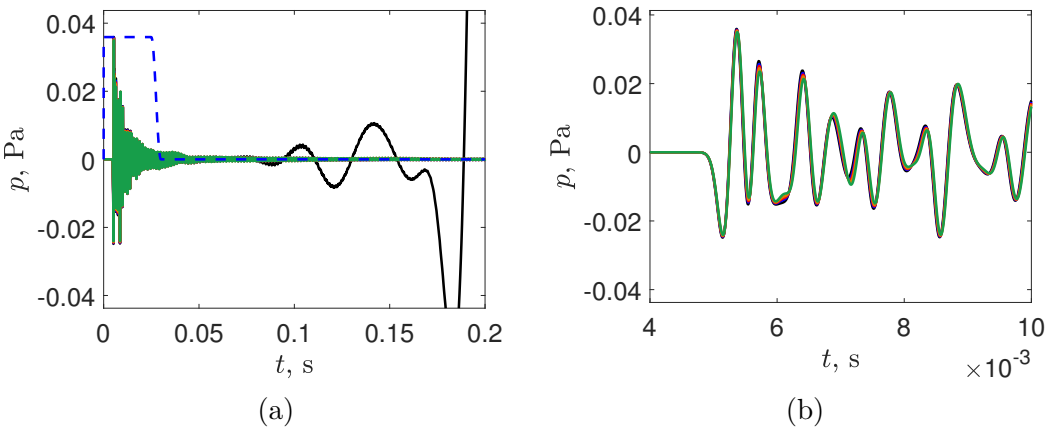

Fig. 25. (a) Time series of pressure on the rigid wall of the large duct at $x = 0.5\,L$ and (b) view for $0.004\text{ s} \leq t \leq 0.01\text{ s}$ for $\epsilon = 1$, $\epsilon = 0.7$, $\epsilon = 0.5$, $\epsilon = 0.3$ and $\epsilon = 0$. The dashed line shows the shape of the window function used in signal processing.

For the large duct, ΔW takes much smaller values. Over the entire frequency band of interest, it is smaller than 3 dB for the full GTS method and than 1 dB for the partial GTS method and for $\epsilon = 0.7$. The results shown in this section confirm that the partial GTS method noticeably impacts the acoustic propagation for low Helmholtz numbers but should be acceptable for large Helmholtz numbers.

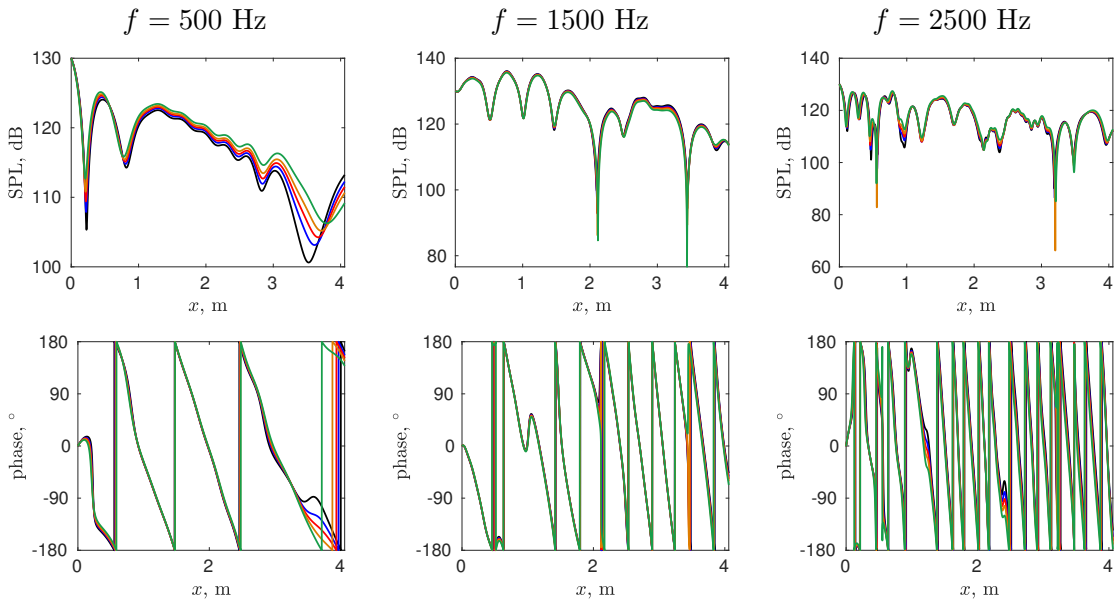

Fig. 26. SPL and phase of the acoustic pressure along the large cross-section duct for $M = 0.335$ and for different values of ϵ: $\epsilon = 1$, $\epsilon = 0.7$, $\epsilon = 0.5$, $\epsilon = 0.3$, $\epsilon = 0$.

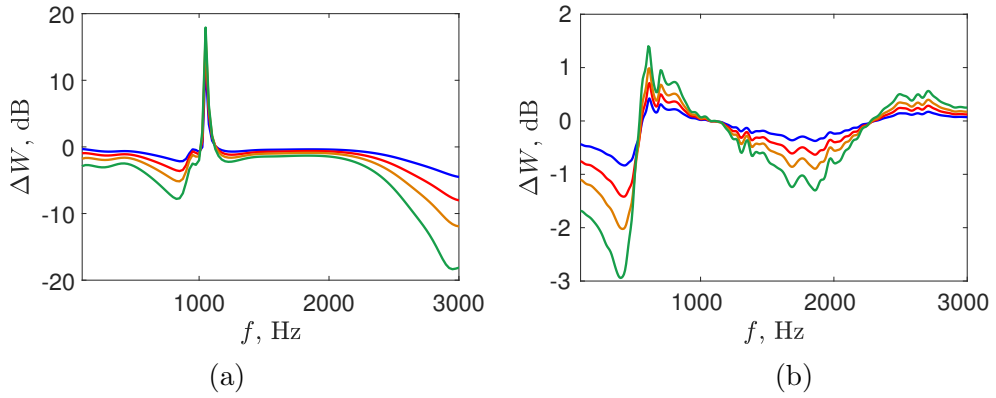

Fig. 27. Power difference $W(\epsilon)/W(\epsilon = 1)$ as a function of the frequency (a) for the NASA GIT duct and (b) for the large duct and for different values of ϵ: $\epsilon = 0.7$, $\epsilon = 0.5$, $\epsilon = 0.3$, $\epsilon = 0$.

6. Conclusion

An analysis of the partial GTS method for suppressing hydrodynamic instabilities in a lined flow duct has been performed. The case of a convective instability generated in a lined flow duct was first illustrated. The instability was calculated by solving the linearized Euler equations with a finite-difference time-domain approach. The characteristics of the instability were compared with the predictions of modal analysis. It was shown that both methods indicate that the instability is convective. Perfect matches of wavenumber and mode shapes were also obtained. The effect of the grid resolution and selective filter, which have been reported in the literature to have a significant impact on the instabilities, was investigated. It turns out that very fine grids, compared with what is required for acoustic waves, are needed for precisely calculating the instability.

The partial GTS method for suppressing the instability was then assessed. The impact of diminishing the mean flow gradient term on the modes has been investigated. The unstable mode turns to be highly sensitive to the mean flow gradient term. The acoustic modes are also greatly altered for small Helmholtz numbers, but are less affected for high Helmholtz numbers. The partial GTS method was finally applied on the NASA GIT benchmark. The effectiveness of this method has been shown for removing the instabilities in time-domain simulations. The SPL was however underestimated by several dBs for certain frequencies. In particular, a total suppression of the mean flow gradient term seems too severe to accurately predict sound propagation in a lined flow duct, while a partial suppression of this term seems to provide an acceptable prediction, especially in the high frequency range.

In addition, even if removing instabilities allows for a stable numerical calculation, it may be, in particular cases, not physically valid: as an example, the feedback mechanism between the instability and acoustic waves for a liner of finite length discussed in Alomar and Aurégan [9] could not be reproduced when the instability is suppressed.

Future works can be conducted to study an absolute instability in the time-domain approach. Since the effectiveness of the partial GTS method has been proved, other techniques proposed for dealing with shear instabilities [40, 41, 42, 44, 43] can also be considered.

Acknowledgments

Y. Deng is sponsored by China Scholarship Council as a Ph.D. student in Ecole Centrale de Lyon. This work was performed within the framework of the Labex CeLyA of the Université de Lyon, within the programme "Investissements d'Avenir" (ANR-10-LABX-0060/ANR-16-IDEX-0005) operated by the French National Research Agency (ANR). The authors would like to thank Dr. Michael Jones (NASA) for providing the data for the NASA GIT benchmark.

Appendix A. Matrices of the discretized eigenvalue problem

This appendix details the discretization of the eigenvalue problem to obtain the mode wavenumber and mode shapes. The number of grid points is denoted by N. Eq. (11) could be rewritten as: $\mathbf{AX} = \frac{k}{\omega}\mathbf{BX}$ with $\mathbf{X}$ being the column vector of unknowns at the grid points:

$$\mathbf{X} = [U(z_1)\cdots U(z_N)\ (P-V)(z_1)\cdots(P-V)(z_N)\ (P+V)(z_1)\cdots(P+V)(z_N)]^T \tag{A.1}$$

where $(z_i)_{1\leq i\leq N}$, with $z_1 = 0$ and $z_N = 1$, are the grid points. At the boundary points, the variables should satisfy both the LEE equations and the boundary conditions. To avoid having an over-constrained system, some information must be discarded. The use of characteristic variables allows one to make a suitable choice. Thus, at $z = 0$, the incident wave on the boundary is $P - V$ and the reflected wave is $P + V$. Therefore, $P + V$ is determined with the boundary condition and not from the LEE. Similarly, at $z = 1$, the incident and reflected wave are $P + V$ and $P - V$, respectively and, hence, $P - V$ is determined with the boundary condition.

Bringing the LEE equations and the boundary conditions together lead to the $3N \times 3N$ matrices:

$$\mathbf{A} = \left[\begin{array}{c|c|c} \mathbf{I}_{(1:N),(1:N)} & -\frac{\epsilon}{2\mathrm{i}\omega}(\mathbf{D}\mathbf{U_0})_{(1:N),(1:N)} & \frac{\epsilon}{2\mathrm{i}\omega}(\mathbf{D}\mathbf{U_0})_{(1:N),(1:N)} \\ \hline \mathbf{0}_{N,N} & \left(\mathbf{I} - \frac{1}{\mathrm{i}\omega}\mathbf{D}\right)_{(1:N-1),(1:N)} & \mathbf{0}_{N-1,N} \\ & 0 \quad \ldots \quad 0 \quad -1-\beta & 0 \quad \ldots \quad 0 \quad 1-\beta \\ \hline \mathbf{0}_{N,N} & 1 \quad 0 \quad \ldots \quad 0 & -1 \quad 0 \quad \ldots \quad 0 \\ & \mathbf{0}_{N-1,N} & \left(\mathbf{I} + \frac{1}{\mathrm{i}\omega}\mathbf{D}\right)_{(2:N),(1:N)} \end{array}\right] \tag{A.2}$$

$$\mathbf{B} = \left[\begin{array}{c|c|c} \mathbf{U_0}_{(1:N),(1:N)} & \frac{1}{2}\mathbf{I}_{(1:N),(1:N)} & \frac{1}{2}\mathbf{I}_{(1:N),(1:N)} \\ \hline \mathbf{I}_{(1:N-1,N)} & \mathbf{U_0}_{(1:N-1),(1:N)} & \mathbf{0}_{N,N} \\ \mathbf{0}_{1,N} & \mathbf{0}_{1,N} & \\ \hline \mathbf{0}_{1,N} & \mathbf{0}_{N,N} & \mathbf{0}_{1,N} \\ \mathbf{I}_{(2:N,N)} & & \mathbf{U_0}_{(2:N),(1:N)} \end{array}\right] \tag{A.3}$$

where $\mathbf{0}_{I,J}$ is the zero matrix with I rows and J columns and $\mathbf{D}$ and $\mathbf{I}$ are the differentiation and identity matrix, respectively, both square matrices of size N. The matrix $\mathbf{U_0}$ is a diagonal matrix of size N with diagonal elements $\mathbf{U_0}_{\,i,i} = u_0(z_i)$. In addition, the notation $\mathbf{M}_{(I:J),(K:L)}$ indicates the submatrix of $\mathbf{M}$ formed by rows I to J and columns K to L. Finally, the parameter ϵ in matrix $\mathbf{A}$ controls the mean flow gradient term and is equal to $\epsilon = 1$ for the LEE equations and to $\epsilon = 0$ for the full GTS method.

Appendix B. Comparison of the instability characteristics for another frequency

In this appendix, the comparison of the instability characteristics determined from the time-domain numerical solution with those predicted by the modal analysis approach, done in Section 3 for $\omega = 0.9271$, is performed for another frequency, namely $\omega = 0.4636$. The objective is to confirm the viability of the time-domain method in simulating the instability.

Fig. B.28 displays the wavenumbers of the modes determined by modal analysis for $\omega = 0.4636$. The reference result $\omega = 0.9271$ is also indicated. Note that the MSD liner model is still used and the liner impedance at these two frequencies is different. The wavenumbers of the acoustic propagating mode ($k = 0.79 - 0.33\mathrm{i}$) and the unstable mode ($k_{\mathrm{HI}} = 2.57 + 1.31\mathrm{i}$) show the most evident change. Compared with $\omega = 0.9271$, the spatial growth rate of the unstable mode decreases only slightly. On the other hand, the wavelength becomes three times longer. Fig. B.29 shows the evolution of $\arg(p)$ and $\ln|p|$ along the lined wall for $\omega = 0.4636$ obtained from the time-domain solution at $t = 90$ and predicted with the analytical solution in Eq. (14), where the value of k_{HI} obtained from modal analysis has been used. Here again, an excellent match is observed.

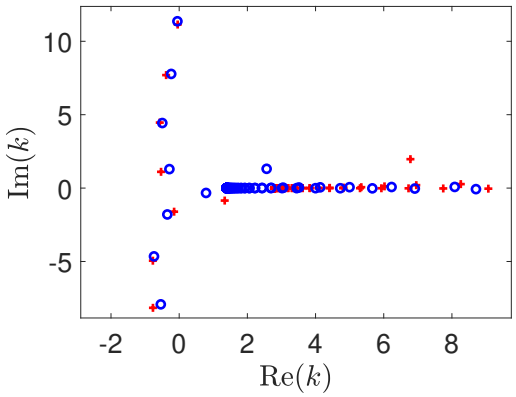

Fig. B.28. Wavenumber obtained by modal analysis for ∘ $\omega = 0.4636$ and + $\omega = 0.9271$.

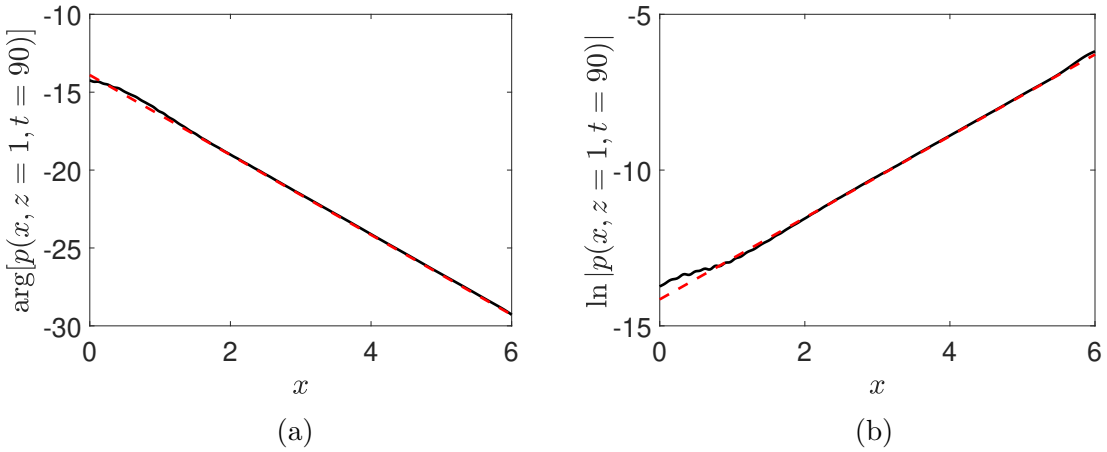

Fig. B.29. Comparison of (a) the phase and (b) amplitude of the pressure on the lined wall for $\omega = 0.4636$ from the time-domain solution at $t = 90$ ——— and from the analytical solution - - - -.

References

[1] Y. Özyörük, L. N. Long, M. G. Jones, Time-domain numerical simulation of a flow-impedance tube, J. Comput. Phys. 146 (1) (1998) 29–57.

[2] H. Ju, K.-Y. Fung, Time-domain impedance boundary conditions with mean flow effects, AIAA J. 39 (9) (2001) 1683–1690.

[3] C. Richter, F. H. Thiele, X. D. Li, M. Zhuang, Comparison of time-domain impedance boundary conditions for lined duct flows, AIAA J. 45 (6) (2007) 1333–1345.

[4] E. Meyer, F. Mechel, G. Kurtze, Experiments on the influence of flow on sound attenuation in absorbing ducts, J. Acoust. Soc. Am. 30 (3) (1958) 165–174.

[5] M. Brandes, D. Ronneberger, Sound amplification in flow ducts lined with a periodic sequence of resonators, Munich, Germany, 1995, pp. 893–901.

[6] Y. Aurégan, M. Leroux, Experimental evidence of an instability over an impedance wall in a duct with flow, J. Sound Vib. 317 (3-5) (2008) 432–439.

[7] Y. Aurégan, D. Kumar Singh, Experimental observation of a hydrodynamic mode in a flow duct with a porous material, J. Acoust. Soc. Am. 136 (2) (2014) 567–572.

[8] D. Marx, Y. Aurégan, H. Bailliet, J.-C. Valière, PIV and LDV evidence of hydrodynamic instability over a liner in a duct with flow, J. Sound Vib. 329 (18) (2010) 3798–3812.

[9] A. Alomar, Y. Aurégan, Particle image velocimetry measurement of an instability wave over a porous wall in a duct with flow, J. Sound Vib. 386 (2017) 208–224.

[10] U. Ingard, Influence of fluid motion past a plane boundary on sound reflection, absorption, and transmission, J. Acoust. Soc. Am. 31 (7) (1959) 1035–1036.

[11] M. Myers, On the acoustic boundary condition in the presence of flow, J. Sound Vib. 71 (3) (1980) 429–434.

[12] B. J. Tester, The propagation and attenuation of sound in lined ducts containing uniform or "plug" flow, J. Sound Vib. 28 (2) (1973) 151–203.

[13] C. K. Tam, L. Auriault, Time-domain impedance boundary conditions for computational aeroacoustics, AIAA J. 34 (5) (1996) 917–923.

[14] S. W. Rienstra, A classification of duct modes based on surface waves, Wave Motion. 37 (2) (2003) 119–135.

[15] S. W. Rienstra, B. J. Tester, An analytic Green's function for a lined circular duct containing uniform mean flow, J. Sound Vib. 317 (3-5) (2008) 994–1016.

[16] X. D. Li, C. Richter, F. Thiele, Time-domain impedance boundary conditions for surfaces with subsonic mean flows, J. Acoust. Soc. Am. 119 (5) (2006) 2665–2676.

[17] E. J. Brambley, Fundamental problems with the model of uniform flow over acoustic linings, J. Sound Vib. 322 (4-5) (2009) 1026–1037.

[18] E. J. Brambley, Well posed boundary condition for acoustic liners in straight ducts with flow, AIAA J. 49 (6) (2011) 1272–1282.

[19] S. Rienstra, G. Vilenski, Spatial instability of boundary layer along impedance wall, in: 14th AIAA/CEAS Aeroacoustics Conference, AIAA Paper 2008–2932, Vancouver, BC, Canada, 2008, pp. 1–13.

[20] Y. Renou, Y. Aurégan, Failure of the Ingard–Myers boundary condition for a lined duct: An experimental investigation, J. Acoust. Soc. Am. 130 (1) (2011) 52–60.

[21] S. Rienstra, Impedance models in time domain, including the extended Helmholtz resonator model, in: 12th AIAA/CEAS Aeroacoustics Conference, AIAA Paper 2006-2686, Cambridge, MA, USA, 2006.

[22] S. W. Rienstra, M. Darau, Boundary-layer thickness effects of the hydrodynamic instability along an impedance wall, J. Fluid Mech. 671 (2011) 559–573.

[23] G. Boyer, E. Piot, J.-P. Brazier, Theoretical investigation of hydrodynamic surface mode in a lined duct with sheared flow and comparison with experiment, J. Sound Vib. 330 (8) (2011) 1793–1809.

[24] D. Marx, A piecewise linear mean flow model for studying stability in a lined channel, J. Sound Vib. 331 (16) (2012) 3809–3823.

[25] D. Marx, Numerical computation of a lined duct instability using the linearized Euler equations, AIAA J. 53 (8) (2015) 2379–2388.

[26] L. Pascal, E. Piot, G. Casalis, Global linear stability analysis of flow in a lined duct, J. Sound Vib. 410 (2017) 19–34.

[27] G. Gabard, E. Brambley, A full discrete dispersion analysis of time-domain simulations of acoustic liners with flow, J. Comput. Phys. 273 (2014) 310–326.

[28] Y. Deng, D. Dragna, M.-A. Galland, A. Alomar, Comparison of three numerical methods for acoustic propagation in a lined duct with flow, in: 25th AIAA/CEAS Aeroacoustics Conference, AIAA Paper 2019-2658, Delft, The Netherlands, 2019, pp. 1–15.

[29] D. Khamis, E. J. Brambley, Viscous effects on the acoustics and stability of a shear layer over an impedance wall, J. Fluid Mech. 810 (2017) 489–534.

[30] D. Marx, Y. Aurégan, Effect of turbulent eddy viscosity on the unstable surface mode above an acoustic liner, J. Sound Vib. 332 (15) (2013) 3803–3820.

[31] J. Rodríguez Sánchez, Étude théorique et numérique des modes propres acoustiques dans un conduit avec écoulement et parois absorbantes, PhD thesis, Toulouse, ISAE (2016).

[32] B. Xin, D. Sun, X. Jing, X. Sun, Numerical study of acoustic instability in a partly lined flow duct using the full linearized Navier–Stokes equations, J. Sound Vib. 373 (2016) 132–146.

[33] R. Sebastian, D. Marx, V. Fortuné, Numerical simulation of a turbulent channel flow with an acoustic liner, J. Sound Vib. 456 (2019) 306–330.

[34] E. Brambley, G. Gabard, Time-domain implementation of an impedance boundary condition with boundary layer correction, J. Comput. Phys. 321 (2016) 755–775.

[35] C. Bogey, C. Bailly, D. Juvé, Computation of flow noise using source terms in linearized Euler's equations, AIAA J. 40 (2) (2002) 235–243.

[36] C. Richter, H. Lueck, L. Panek, F. Thiele, Methods for suppressing shear layer instabilities for CAA, J. Comput. Acoustics 19 (02) (2011) 181–203.

[37] Y. Özyörük, B. J. Tester, Application of frequency-domain linearized Euler solutions to the prediction of aft fan tones and comparison with experimental measurements on model scale turbofan exhaust nozzles, J. Sound Vib. 330 (16) (2011) 3846–3858.

[38] A. Iob, R. Arina, C. Schipani, Frequency-domain linearized Euler model for turbomachinery noise radiation through engine exhaust, AIAA J. 48 (4) (2010) 848–858.

[39] X. Li, C. Schemel, U. Michel, F. Thiele, Azimuthal sound mode propagation in axisymmetric flow ducts, AIAA J. 42 (10) (2004) 2019–2027.

[40] R. Ewert, W. Schröder, Acoustic perturbation equations based on flow decomposition via source filtering, J. Comput. Phys. 188 (2) (2003) 365–398.

[41] J.-H. Seo, Y. J. Moon, Perturbed compressible equations for aeroacoustic noise prediction at low Mach numbers, AIAA J. 43 (8) (2005) 1716–1724.

[42] J. H. Seo, Y. J. Moon, Linearized perturbed compressible equations for low Mach number aeroacoustics, J. Comput. Phys. 218 (2) (2006) 702–719.

[43] X. Zhang, X. Chen, J. Gill, Gradient term filtering for stable sound propagation with linearized Euler equations, in: 20th AIAA/CEAS Aeroacoustics Conference, AIAA Paper 2014-3306, Atlanta, GA, 2014, pp. 1–14.

[44] Y. Sun, R. Fattah, S. Zhong, X. Zhang, Stable time-domain CAA simulations with linearised governing equations, Comput. Fluids. 167 (2018) 187–195.

[45] C. Bogey, C. Bailly, A family of low dispersive and low dissipative explicit schemes for flow and noise computations, J. Comput. Phys. 194 (1) (2004) 194–214.

[46] J. Berland, C. Bogey, O. Marsden, C. Bailly, High-order, low dispersive and low dissipative explicit schemes for multiple-scale and boundary problems, J. Comput. Phys. 224 (2) (2007) 637–662.

[47] J. Berland, C. Bogey, C. Bailly, Low-dissipation and low-dispersion fourth-order Runge–Kutta algorithm, Comput. Fluids. 35 (10) (2006) 1459–1463.

[48] C. Bogey, N. de Cacqueray, C. Bailly, A shock-capturing methodology based on adaptative spatial filtering for high-order non-linear computations, J. Comput. Phys. 228 (5) (2009) 1447–1465.

[49] C. Bogey, C. Bailly, Three-dimensional non-reflective boundary conditions for acoustic simulations: far field formulation and validation test cases, Acta Acust. united Ac. 88 (2002) 463–471.

[50] R. Troian, D. Dragna, C. Bailly, M.-A. Galland, Broadband liner impedance eduction for multimodal acoustic propagation in the presence of a mean flow, J. Sound Vib. 392 (2017) 200–216.

[51] B. Gustavsen, A. Semlyen, Rational approximation of frequency domain responses by vector fitting, IEEE Trans. Power Deliv. 14 (3) (1999) 1052–1061.

[52] L. N. Trefethen, Spectral methods in MATLAB, Vol. 10, Siam, 2000.

[53] E. J. Brambley, M. Darau, S. W. Rienstra, The critical layer in linear-shear boundary layers over acoustic linings, J. Fluid Mech. 710 (2012) 545–568.

[54] G. G. Vilenski, S. W. Rienstra, Numerical study of acoustic modes in ducted shear flow, J. Sound Vib. 307 (3-5) (2007) 610–626.

[55] R. Briggs, Electron–stream interaction with plasmas, MIT Press, Cambridge, 1964.

[56] P. Huerre, P. A. Monkewitz, Local and global instabilities in spatially developing flows, Annual review of fluid mechanics 22 (1) (1990) 473–537.

[57] E. J. Brambley, N. Peake, Classification of aeroacoustically relevant surface modes in cylindrical lined ducts, Wave Motion. 43 (4) (2006) 301–310.

[58] M. Jones, W. Watson, T. Parrott, Benchmark data for evaluation of aeroacoustic propagation codes with grazing flow, in: 11th AIAA/CEAS Aeroacoustics Conference, AIAA Paper 2005-2853, Monterey, CA, USA, 2005, pp. 1–18.

[59] M. O. Burak, M. Billson, L.-E. Eriksson, S. Baralon, Validation of a time- and frequency-domain grazing flow acoustic liner model, AIAA J. 47 (8) (2009) 1841–1848.